Energy Balance From a Mantle Pseudotachylyte, Balmuccia, Italy

Thomas Ferrand, Loïc Labrousse, Grégoire Eloy, Olivier Fabbri, Nadege Hilairet, Alexandre Schubnel

AGU100 ADVANCING EARTH AND SPACE SCIENCE

JGR

Journal of Geophysical Research: Solid Earth

RESEARCH ARTICLE
10.1002/2017JB014795

Key Points:
- The studied pseudotachylyte is the fossilized trace of an earthquake which occurred in the mantle, > 40 km deep; its magnitude was >6
- Coseismic total melting leads to complete fault lubrication; the ultramafic melt flows in "injection" veins, inducing fault restrengthening
- Micrometric crystals, forming during fault restrengthening, record the sliding history, *P-T* conditions, and focal mechanism of the earthquake

Correspondence to:
T. P. Ferrand,
ferrand@geologie.ens.fr

Citation:
Ferrand, T. P., Labrousse, L., Eloy, G., Fabbri, O., Hilairet, N., & Schubnel, A. (2018). Energy balance from a mantle pseudotachylyte, Balmuccia, Italy. *Journal of Geophysical Research: Solid Earth*, *123*, 3943–3967. https://doi.org/10.1002/2017JB014795

Received 28 JUL 2017
Accepted 21 MAR 2018
Accepted article online 25 MAR 2018
Published online 12 MAY 2018

Energy Balance From a Mantle Pseudotachylyte, Balmuccia, Italy

Thomas P. Ferrand[1], Loïc Labrousse[2], Grégoire Eloy[1], Olivier Fabbri[3], Nadège Hilairet[4], and Alexandre Schubnel[1]

[1]Laboratoire de Géologie – UMR 8538, CNRS, Ecole Normale Supérieure, PSL★ Research University, Paris, France, [2]Institut des Sciences de la Terre de Paris – UMR 7193, CNRS, Université Pierre et Marie Curie, Paris, France, [3]Laboratoire Chrono-environnement – UMR 6249, CNRS, Université Bourgogne – Franche-Comté, Besançon, France, [4]Univ. Lille, CNRS, INRA, ENSCL, UMR 8207 - UMET - Unité Matériaux et Transformations, Lille, France

Abstract In the Balmuccia massif (NW Italy), a pseudotachylyte vein network (N068 trending) in a spinel lherzolite is interpreted as the product of frictional melting during a single $M_w > 6$ earthquake. The subvertical fault underwent a metric dextral coseismic displacement, raking 60°SW. The average width of the main slip surface is ~ 5 mm. A dense network of thin (20–200 μm) injection and ultramylonite-like veins decorates the fault walls. In the injection veins, Raman microspectrometry mapping reveals pockets of still preserved amorphous silicate, containing ≈ 1% of structurally bound H_2O. In the ultramylonite-like veins, electron backscattered diffraction mapping reveals that ultrafine (0.2–2 μm) olivine grains exhibit a strong fabric with (010) planes parallel to shearing, consistent with temperatures above 1250°C during deformation and suggesting fast recrystallization from the frictional melt. The veins also exhibit pyroxene and recrystallized spinel, which proves that the earthquake occurred at a minimum depth of 40 km. The energy balance demonstrates that complete fault lubrication must have occurred during coseismic sliding (i.e., dynamic friction coefficient $\ll 0.1$). Because of the low viscosity of slightly hydrated ultramafic liquids (≈ 1 Pa·s), we argue that lubrication was only transient, as the melt could rapidly flow into tensile fractures, which led to rapid cooling and promoted strength recovery and sliding arrest. Combined together, our observations suggest that this pseudotachylyte is the frozen record of a deep (>40 km) earthquake of $6 < M_w < 7$. Its focal mechanism is deduced from the crystal preferred orientation due to late coseismic creep in ultramylonite-like veins and deciphered by electron backscattered diffraction.

Plain Language Summary In active mountain ranges, rocky massifs gradually rise to the surface under the combined effect of convergence and erosion. It is then possible to observe in the field the fossilized traces of earthquakes that have occurred several kilometers deep, tens of millions of years ago. Thus, it can be seen that contrary to what we experience on the surface, the rock melts when it tears. A magma forms and facilitates relative ground displacement. The traces discovered by the geologists are the solidified remains of this magma. Here by field observation and detailed analysis of samples in the laboratory, we describe the traces of an earthquake that occurred more than 40 km deep in the Earth's mantle. Its magnitude was greater than 6, the sliding on the fault greater than 1 m, and yet the trace is thinner than 5 mm. And, against all odds, the most talkative witnesses are extremely small: micrometric crystals, which formed from the magma upon the rupture, record crucial information unveiling its focal mechanism. We still do not entirely know what an earthquake exactly is, and nobody will ever be able to see what happens on the fault at depth during an earthquake. Hence, these fossils are key.

1. Introduction

Pseudotachylytes were originally thought to result from local melting of rocks on the surface of faults due to heat generated by frictional sliding (Philpotts, 1964; Sibson, 1975), also known as flash melting (e.g., Beeler et al., 2008; Rempel, 2006; Rice, 2006). The formation of pseudotachylytes (solidified frictional melt) is now thought to attest to coseismic fault lubrication. Melting would be one possible slip-weakening mechanism associated with the propagation of seismic ruptures (e.g., Bouchon & Ihmlé, 1999; Kanamori et al., 1998), during which coseismic slip velocities can reach 1–10 m/s (Di Toro et al., 2006; Hirose & Shimamoto, 2005a). Pseudotachylytes associated with exhumed regional fault zones can be used as an indicator for paleoseismicity (Sibson, 1975).

The Balmuccia peridotite, northwestern Italian Alps, where many pseudotachylyte veins have been observed (Obata & Karato, 1995; Souquière et al., 2011; Souquière & Fabbri, 2010; Ueda et al., 2008), provides an excellent opportunity to investigate the mechanics of upper mantle earthquakes. At high temperatures, above 1000°C, the mantle deforms relatively homogeneously within domains ranging in size between a few kilometers and a few tens of kilometers. In contrast, below 900°C, deformation is thought to be accommodated by anastomosing networks of centimeter- to hundred-meter-wide mylonitic shear zones, possibly hydrated (Drury et al., 1991).

The Balmuccia peridotite was recently deformed in a rotary-shear apparatus (Del Gaudio et al., 2009) to investigate dynamic fault strength and frictional melting processes in mantle rocks. These laboratory experiments revealed that melt lubrication of this nominally anhydrous rock (Di Toro et al., 2006; Hirose & Shimamoto, 2005a) is the weakening mechanism, probably initiated by flash heating of asperities on the fault surface (Beeler et al., 2008; Rempel, 2006; Rice, 2006). A continuous melt-rich layer formed with an estimated temperature reaching 1780°C (Del Gaudio et al., 2009). With an imposed slip rate around 1 m/s, strengthening occurs at the initiation of sliding with a typical friction coefficient of 0.7 but then decreases down to a steady-state value as low as 0.15 due to lubrication (Del Gaudio et al., 2009). Steady-state shear stress is well below the prediction of Byerlee's law and does not vary much with normal stress (Del Gaudio et al., 2009; Di Toro et al., 2006; Hirose & Shimamoto, 2005a). Theoretical predictions (Nielsen et al., 2008) suggest steady-state shear stresses as low as a few megapascals when ultramafic melts lubricate faults in peridotite-bearing rocks at mantle depths.

Field-based studies in spinel-plagioclase peridotite in Corsica have evidenced very high strengths and stress drops associated with pseudotachylyte generation (Andersen et al., 2008), suggesting that the stresses in small faults (< 5 cm) were very large (200–500 MPa) during the initial fracture propagation, whereas larger faults reveal a much smaller dynamic shear stress integrated over the entire displacement (~10 MPa).

Here we propose to compare energy balances deduced from field observations in the Balmuccia peridotite and from current seismological observations. This multiscale study provides information allowing to decipher the sliding history and focal mechanism of the frozen earthquake, and to estimate its magnitude as performed in previous studies (e.g., Andersen et al., 2014).

2. Geological Setting

2.1. The Ivrea-Verbano Zone

In several mountain belts around the Mediterranean Sea, inheritance of Tethyan rifting is preserved. In particular, rocks from the lower continental crust and the upper mantle were first exhumed by hyperextension and then incorporated into the Alpine orogen (Vissers et al., 1995, and references therein). The Ivrea-Verbano Zone (Figure 1) shows well-preserved preorogenic and orogenic structures exhumed during the Alpine collision along the Insubric Line, which is an inherited tectonic contact formed during the Triassic or before (Mohn et al., 2014). The Ivrea-Verbano Zone was originally the deepest part of a fragmented piece of Paleozoic continental crust (Handy & Stünitz, 2002). Shallower levels of this continental section are exposed in adjacent units to the SE (Strona Ceneri Zone) and NW (Sesia Zone, Figure 1; Handy & Stünitz, 2002; Rutter et al., 2007; Wolff et al., 2012).

The continental crust was first affected by an Early Permian transtension and then by the early Mesozoic rifting, respectively associated with the opening of the Tethys and Liguro-Tethyan ocean basins (Handy & Zingg, 1991). The Ivrea-Verbano Zone was verticalized by the Alpine transpression along the Insubric Line (Figure 1) and nowadays exposes from east to west a cross section of the middle to lower continental crust (Handy et al., 1999; Zingg et al., 1990, and references therein). The Cenozoic deformation was brittle and preserved part of the precollisional fabrics and mineral assemblages (Schmid et al., 1989).

2.2. The Balmuccia Peridotite

The Balmuccia peridotite (Figure 1) is located in the Val Sesia (NW Italy). It mostly consists of spinel lherzolite and spinel harzburgite (< 46 wt% SiO_2, Obata & Karato, 1995). The Balmuccia spinel peridotite is a lens of 5×0.8 km in size (Figure 2). This lens is inherited from a long tectonic activity, that is, exhumation along the Insubric Line, since it was located at mantle depth before the Alpine collision (Quick et al., 1995).

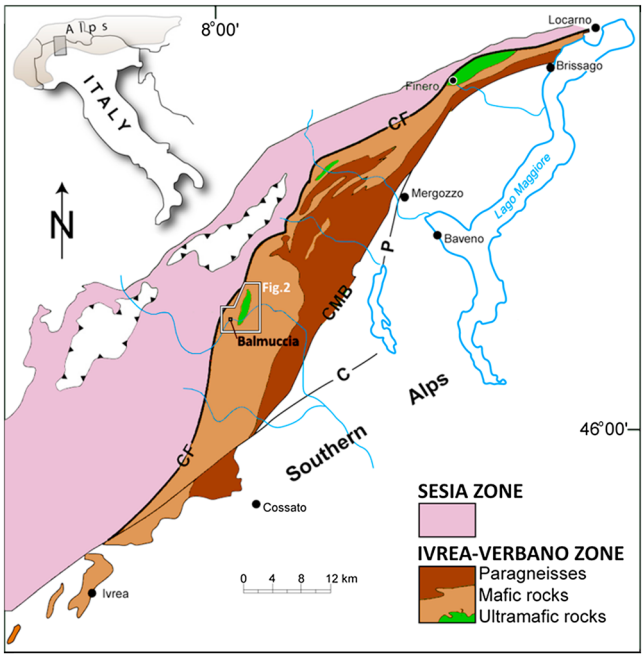

Figure 1. Tectonic map of the Ivrea-Verbano Zone (modified after Zingg, 1983). Major tectonic discontinuities are the Canavese fault (CF, local expression of the Insubric Line), the Cossato-Mergozzo-Brissago fault (CMB), the Pogallo fault (P) and the Cremosina fault (C).

Layers of pyroxenite emplaced ~300 Ma ago (Handy et al., 1999) at 39 ± 5 km depth (Rivalenti et al., 1981, 1984; Shervais, 1979; Sinigoi et al., 1994) near the former Moho (Boudier et al., 1984). Deep crustal extensional faulting is reported in the Ivrea-Verbano Zone (Brodie & Rutter, 1987) and is usually attributed to Permian transtension and to early Jurassic rifting of the Liguro-Tethyan Ocean (Handy & Stünitz, 2002). Exhumation and transtension were followed by Cenozoic brittle deformation along the Insubric Line during the Alpine convergence (Handy et al., 1999). Contrary to the neighboring Sesia zone (Babist et al., 2006), the Ivrea-Verbano Zone was not buried in the subduction wedge and preserves intermediate-depth strain.

Numerous pseudotachylytes have been described in the Balmuccia peridotite lens (Obata & Karato, 1995; Souquière & Fabbri, 2010; Ueda et al., 2008). According to Souquière and Fabbri (2010), two types of pseudotachylyte veins can be distinguished: the "A-type" pseudotachylyte veins are attributed to the latest stages of the Variscan orogeny or to the subsequent Permian transtension broadly between 350 and 270 Ma; "B-type" pseudotachylyte veins were formed later during the Alpine collision (Souquière & Fabbri, 2010). The Balmuccia lens emplaced into granulite facies metabasites of the Ivrea-Verbano Zone in the late Paleozoic (251 Ma ago), before the South Alpine plate separated from Europe (Ernst, 1978; Lensch, 1971; Rivalenti et al., 1975; Shervais, 1979; Shervais & Mukasa, 1991). Thus, spinel-bearing A-type pseudotachylyte veins likely formed before the emplacement of the mantle slice into the lower crust (Ueda et al., 2008).

2.3. Outcrop Locality

The studied outcrop (45°49.2′N, 8°09.3′E) is located in the southern end of the Balmuccia peridotite exposure, along the Sesia River (Figure 3). There, the pyroxenite layers are parallel to the subvertical N002 striking foliation of the peridotite and are offset by a fault system, containing the studied pseudotachylyte. The presently vertical foliation of the peridotite was probably originally horizontal (Rivalenti et al., 1975) like the regional gneissic layering, the whole Ivrea crustal section being rotated along a N-S horizontal axis (Handy et al., 1999; Zingg et al., 1990). Nearly horizontal outcrops along the Sesia River hence show originally vertical cross sections within the peridotite body.

3. Field and Microstructural Observations

3.1. Evidence of Faulting

The studied pseudotachylyte network appears as two black linear traces (Figure 3), which are the intersections of two connected fault planes with the outcrop surface. These faults are subvertical. The major fault segment (branch 1), striking N080, is 35 m long and shows a dextral separation of crosscut markers ranging from 1.2 m, to the west, to 0.8 m, to the east (Figure 4); branch 2, striking N095, near the escarpment, displays an apparent 0.1- to 0.2-m dextral offset. The downstream part of the outcrop shows minimum offset along branch 1 and maximum offset along branch 2. The total strike-slip component is 1–1.2 m. The average width of the pseudotachylyte (branch 1 + branch 2 + smaller embranchments, Figure 4b) is ~5 mm.

The slip history reconstruction (Figure 5) is hindered because the vertical component cannot be readily determined. By geometry, identifying sequences of pyroxenite layers allows to calculate the thickness of the missing peridotite between the northern and southern parts of the outcrop, that is, consumed by the faulting process. Considering a minimal sliding, that is, horizontal, the thickness w of the molten zone should be ~25 cm; if the sliding is oblique, w can be as low as 1 cm. The real thickness lies between these extreme values. Furthermore, the large injection vein is subhorizontal (N050–20S). If injection veins open as tensile fractures orthogonal to the principal stretching axis during coseismic strain, then this large injection vein (green on Figure 3) implies subvertical rupture propagation and thus a significant vertical

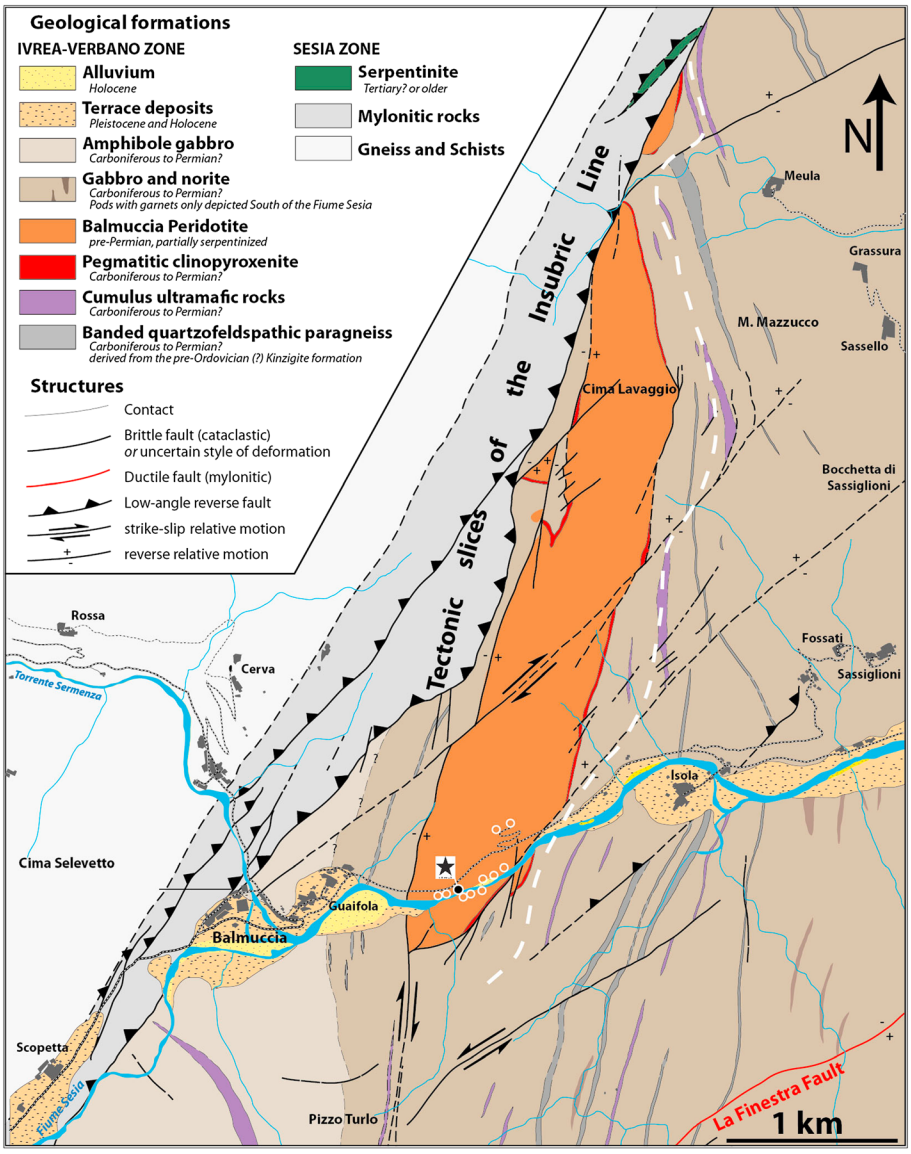

Figure 2. Simplified geological map of the Balmuccia massif (modified after Quick et al., 2003). Ultramafic pseudotachylytes (white circles) are common along the Sesia River. The studied high-pressure exposure (Figure 3) is located by the black star.

component of slip. The northern half-space would have moved up compared to the southern part (Figure 5b), as for a large majority of regional faults in the Balmuccia region (Handy & Stünitz, 2002; Quick et al., 2003).

Branch 1 and branch 2 merge to the east of the outcrop (Figure 3). Along with small-scale embranchments (Figure 4a), they delimit millimetric to metric lenses. Most branches of this anastomosed network are connected. Some crosscutting relationships can be seen at millimeter scale but only locally and without any systematic trend. As the geometry of the pseudotachylyte vein network does not show any evidence of repeated deformation events, it is reasonable to consider that the fault network recorded only one seismic event. The relay zone shows multiple offsets in the pyroxenite layers. The millimetric to centimetric strike-slip components in the relay zone show both dextral and sinistral senses of shear, which could be due to a merging-induced space problem along with a substantial vertical component on the main slip surfaces. Downstream, the principal fault seems to extend in an inaccessible cliff, and a fault fan is visible over some meters before disappearing in the Sesia River. Besides, the geometry of the outcrop differs from a convex erosion surface on the river side (south) to a quasi-perfect plane on the cliff side (north). The latter,

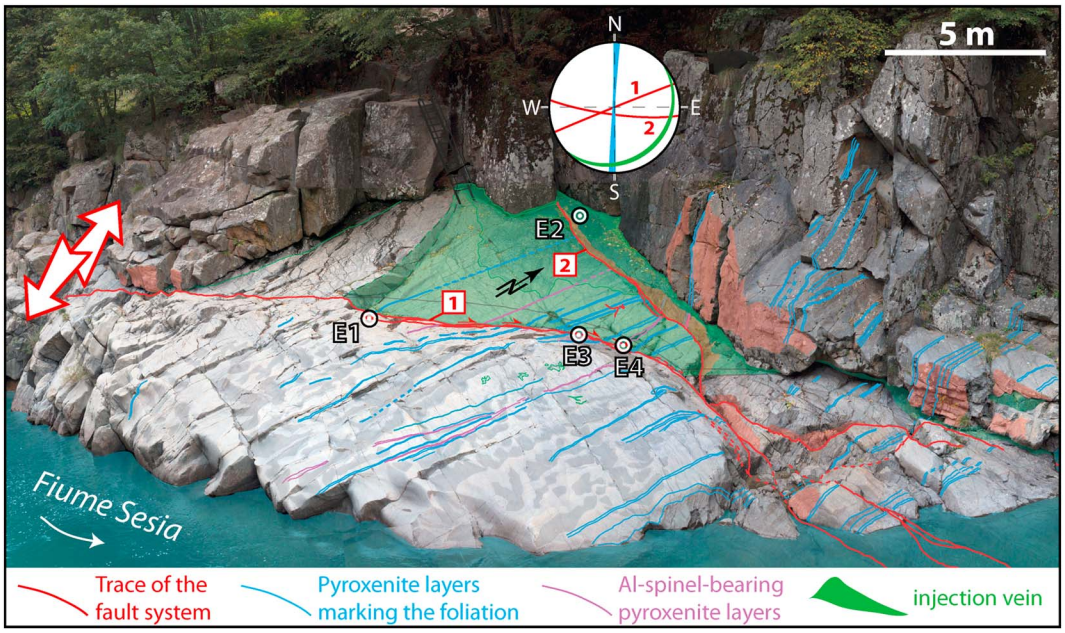

Figure 3. View of the outcrop from the right bank of the Sesia River, with location of the samples discussed in text. Both faults (branch 1 and branch 2, red numbers) and foliation are subvertical. Their intersections with the outcropping surface are indicated by red and blue lines. Thinner olivine websterite layers (≈ 1 cm thick) are not shown here. Purple lines indicate some subvertical layers of Al-spinel-bearing Al-rich pyroxenite. Transparent red indicates near-fault surface. Transparent green shows the injection vein described in the text, which is highly eroded but displays remnants on the bottom surface of the tensile fracture. Stereographic projection is given using lower hemisphere. Scale bar relates to the center of the picture. Arrows illustrate sliding direction and sense of shear.

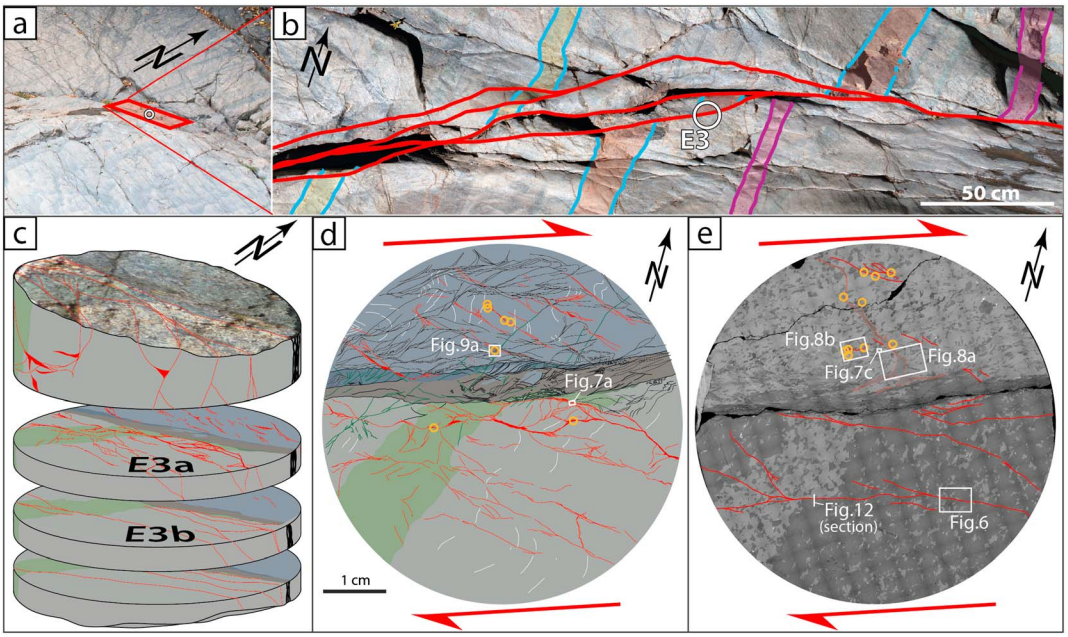

Figure 4. Closer view of the fault trace down to millimeter scale. The fault segment is located in (a) and interpreted in (b). Pyroxenite layers reveal a 0.8 to 1.2 m dextral strike-slip offset component on the main fault trace. The pseudotachylyte is ≈ 5 mm thick on average and is locally composed of several branches. Core sample E3 is shown in (c). Polished surfaces (d) and (e) display the highly altered pseudotachylyte core (brown) separating websterite (blue) from olivine websterite (green) and peridotite (gray). A dense network of ultramylonite-like veins (submicrometric to micrometric grains, red, Figure 6) is surrounded by a population of amorphous pockets (measurement locations indicated with orange circles, details in Figures 7 and 8). Some preseismic localization of the deformation is noticeable (d, dark blue). Red arrows show horizontal shear component. White lines (d) indicate the foliation of the peridotite.

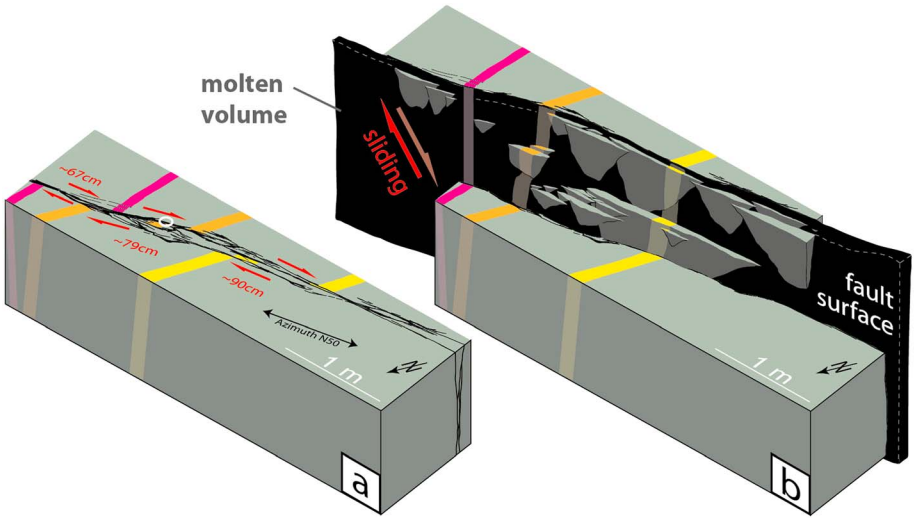

Figure 5. Sketches illustrating the sliding history on the fault segment presented in Figure 4 assuming a 5-cm-thick melt layer. (a) Three-dimensional representation of the fault segment on near-present-day surface; (b) situation of this surface before the earthquake. Sliding N068-60SW.

adorned with black cladding similar to the fault gouge, is here interpreted as the lower wall of a large injection vein, which continues below the cliff (Figure 3).

As revealed by microstructural imaging, the damage zone extends ~10 cm around the main slip surface and consists of a dense network of thin (20–200 μm, Figures 4 and 6) faults and injection veins rooting in this principal slip surface. Nanometric to micrometric grains of olivine, pyroxenes, and spinel fill both the fault (Figures 6, 7a, and 7b) and injection veins (Figures 7c and 7d). Moreover, clasts are hardly present in these fault veins, showing very rare remnants of the wall-rock fabric. The thin fault vein network of the damage zone was turned into micrometric shear zones producing a well-sintered ultrafine-grained texture undistinguishable from textures that would result from intense grain size reduction in solid-state ultramylonites. We therefore refer to them as "ultramylonite-like veins." Similar crystalline aggregates have recently been described in another mantle pseudotachylyte in Lanzo (Scambelluri et al., 2017). Even if we describe in this study how melting is involved in the formation of these veins, we show that it ends with a final solid-state viscous flow, which could be referred to as "late coseismic" or "early postseismic" creep depending on the scale at which the sliding evolution is described. For the sake of clarity, we only mention "late coseismic creep" throughout the paper, considering the whole dynamic process. The damage zone also contains semibrittle and ductile deformation (SC fabric, thin black lines in Figure 4d), as already described in Holsnøy (Aasen, 2013) and Corsica (Silkoset, 2013). This deformation is denser in the blocks located between the pseudotachylyte branches and is likely to have developed during the dynamic rupture propagation and just before crack opening.

3.2. Evidence of Melting

Under dry conditions and atmospheric pressure, melting temperatures are around 1400°C for diopside, 1550°C for enstatite, 1700°C for olivine, and 1850°C for spinel (Philpotts, 1990; Spray, 1992). Considering little hydration during sliding, the average peak temperature to melt peridotite is close to 1800°C, as measured in rotary-shear experiments (Del Gaudio et al., 2009).

Raman spectrometry in micrometric injection veins reveals amorphous material (Figure 8). Most of this amorphous material is observed embedded within healed fractures in diopside crystals, most of which are part of the pyroxenite layers. A significant part of the damage caused by the dynamic rupture must have consisted of small fractures affecting crystals, as evidenced by cathodoluminescence studies in pseudotachylytes, showing that pervasive cataclastic networks of healed fractures are missed by classical investigation techniques (Bestmann et al., 2012, 2016). Considering minimal relative displacement, these cracks should easily heal by diffusion above 800°C, except if the silicate melt, coming from total melting on the fault plane, is emplaced during crack opening.

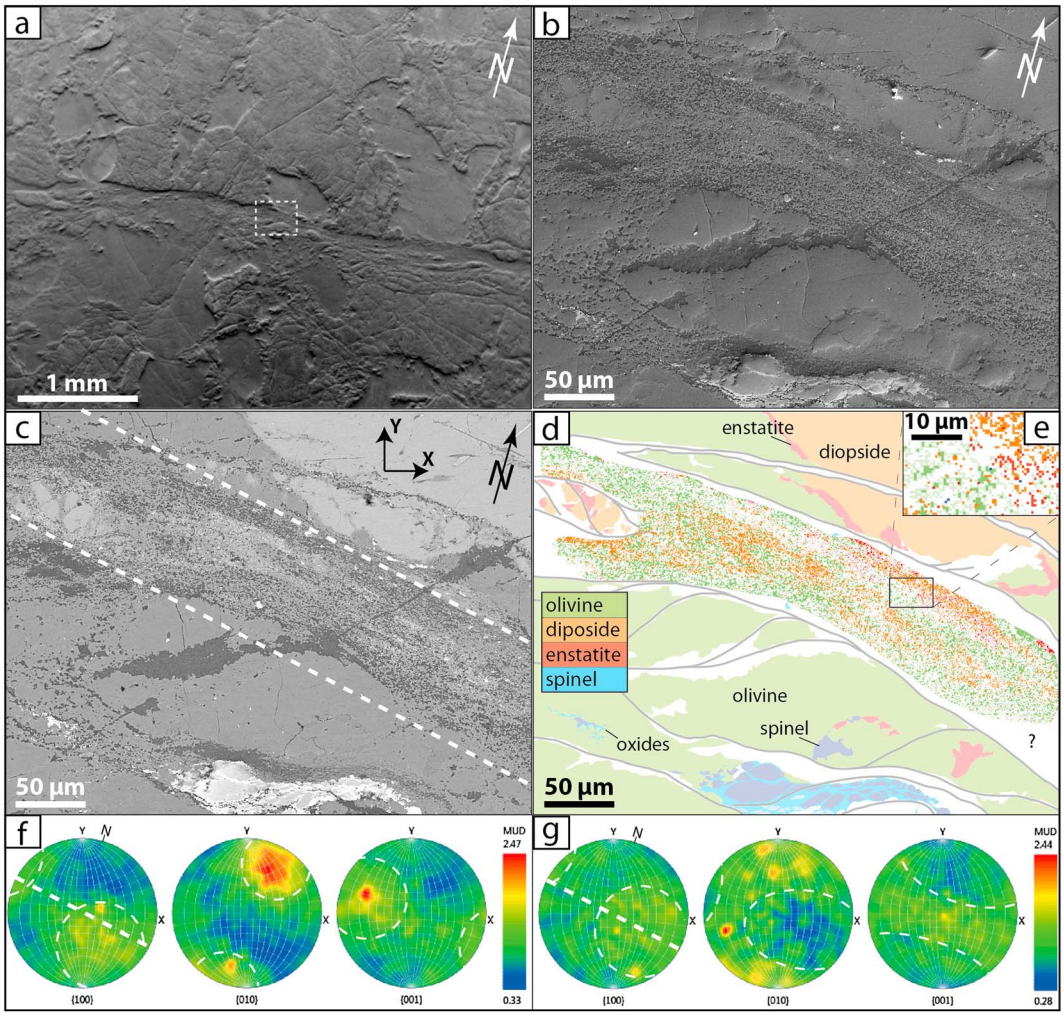

Figure 6. Microscale observations on sample E3 using electron backscatter diffraction (EBSD). (a) Scanning electron microscope (SEM) image (forward scatter detector) of a thin ultramylonite-like vein (≈ 100 µm thick), representative of the network of microfaults (20 to 200 µm thick); (b) SEM SE2 image (secondary electrons) closer to the vein; (c) SEM density contrast (backscattered electrons); (d) drawing showing main structures and composition, along with the vein content on an area of ≈ 400 μm^2; These faults are filled with crystals of olivine (≈ 41 vol.%, green), diopside (≈ 15 vol.%, orange), enstatite (≈ 41 vol.%, red), and spinel (< 1 vol.%, dark blue), with maximum grain size of 2 µm, and some deformed clasts; (e) closer view on the fault vein; (f) EBSD pole figures for micro-olivine indexed in (d), with [010] axis normal to the fault plane and clear texture of [100] and [001] axes; (g) EBSD pole figures for microdiopside indexed in (d), showing that olivine and diopside [100] axes are subparallel, that is, broadly in the sliding direction. The faults are near perpendicular to the polished surface. Location in Figure 2. Upper stereographic projection. MUD = multiples of uniform distribution. Analysis points number: 87093. Indexation: 61.08%. Olivine: 79.98%; diopside: 24%; enstatite: 2.5%; spinel: 0.05%.

The pluricentimetric injection vein in sample E3b (Figures 8a and 10a, located in Figure 4e) is Na-free and filled with micrometric spinel, olivine, and pyroxene. Glassy material is observed in micrometric pockets around injection and fault veins (Figures 7d and 8c). Near the main fault surface, the Raman signal in the pockets is similar to the one of experimental glass with average peridotite composition (Figure 9). Around the tail of centimetric injection veins, the composition is close to plagioclase (Figure 10) and the Raman signal is close to that of extraterrestrial shocked plagioclase (Freeman et al., 2008). Furthermore, these pockets have a bytownite composition [$(Ca_{0.7},Na_{0.3})AlSi_3O_8$], whereas the host diopsides contain ~ 0.01% Na. In other terms, under these *P-T* conditions, Na^+ is enriched in the residual melt during fractionated crystallization of olivine, pyroxene, and spinel.

A vitrophyric texture is observed in an injection vein (Figure 7c), showing micrometric pyroxenes and spinel nucleating from the melt. Besides, the observation of symplectites around another injection vein (Figure 11) means that two crystals started to grow at the same place through a solid-solid transformation. These symplectites are also Na-free and are made of olivine, spinel, and pyroxene. They might

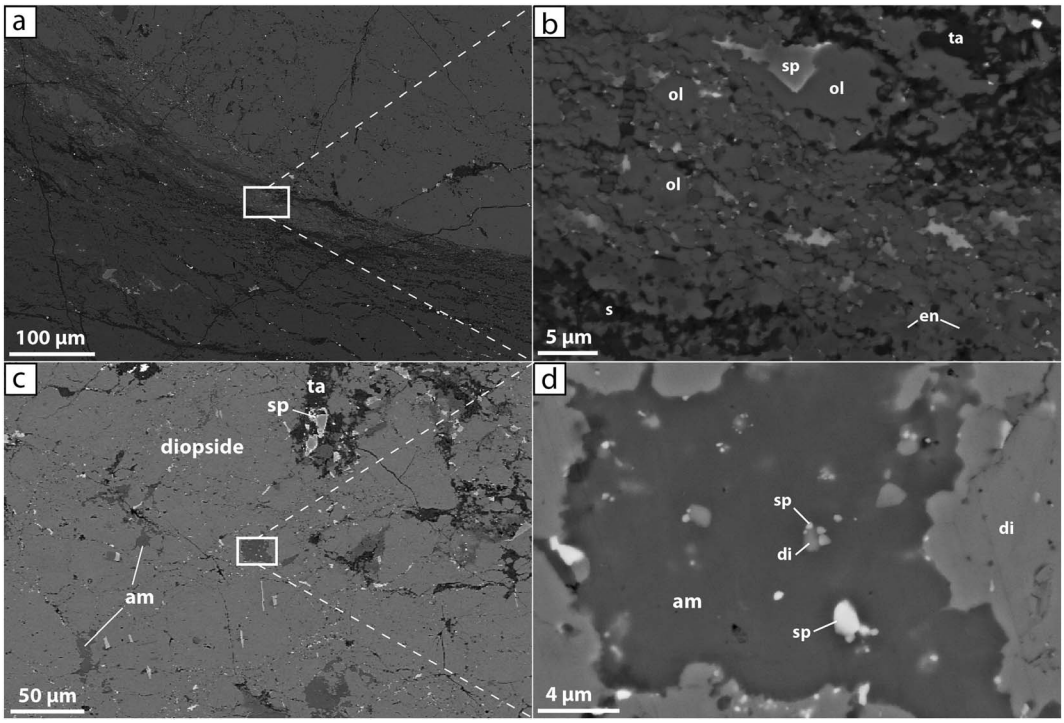

Figure 7. Recrystallized Al-spinel. Stable spinel in an ultramylonite-like vein (a, b) in sample E3a (Figure 4d) and in amorphous pocket (c, d) in sample E3b (Figure 4e). The amorphous pocket (d) shows a vitrophyric texture of submicrometric pyroxene (light gray) and spinel (white). am = amorphous material, di = diopside, sp = Al-spinel, ol = olivine, en = enstatite, ta = talc, and s = serpentine.

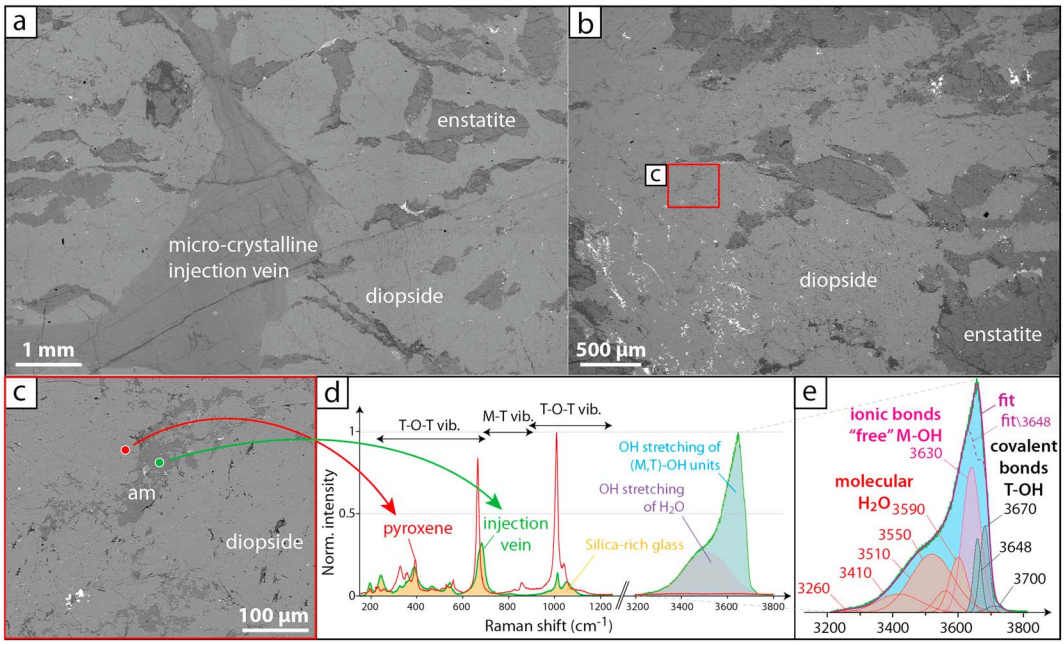

Figure 8. Cryptocrystalline injection veins and amorphous pockets. Scanning electron microscope observations in the micrometric injection vein (sample E3b, Figure 4e). The injection vein (a) is inside a segment of a pyroxenite layer, that is, clinopyroxenes (cpx) and orthopyroxenes (opx). Apparently fully crystalline, it consists of olivine, pyroxene, and Al-spinel in nonaltered zones but also of alteration products such as talc, chlorite, and low-grade serpentine. Amorphous pockets (am) occupy the periphery of the injection vein (b). The pockets (c) are entirely preserved in unaltered diopside grains (cpx). Some small injection veins underwent alteration and devitrification and show hydrous minerals (Figure 11). Normalized Raman spectra of the amorphous material (d, injection vein, green curve/green dot), reveals a water content of ≈ 1.5 wt%, mostly structurally bound (≈ 1%; e, ionic and covalent bonds).

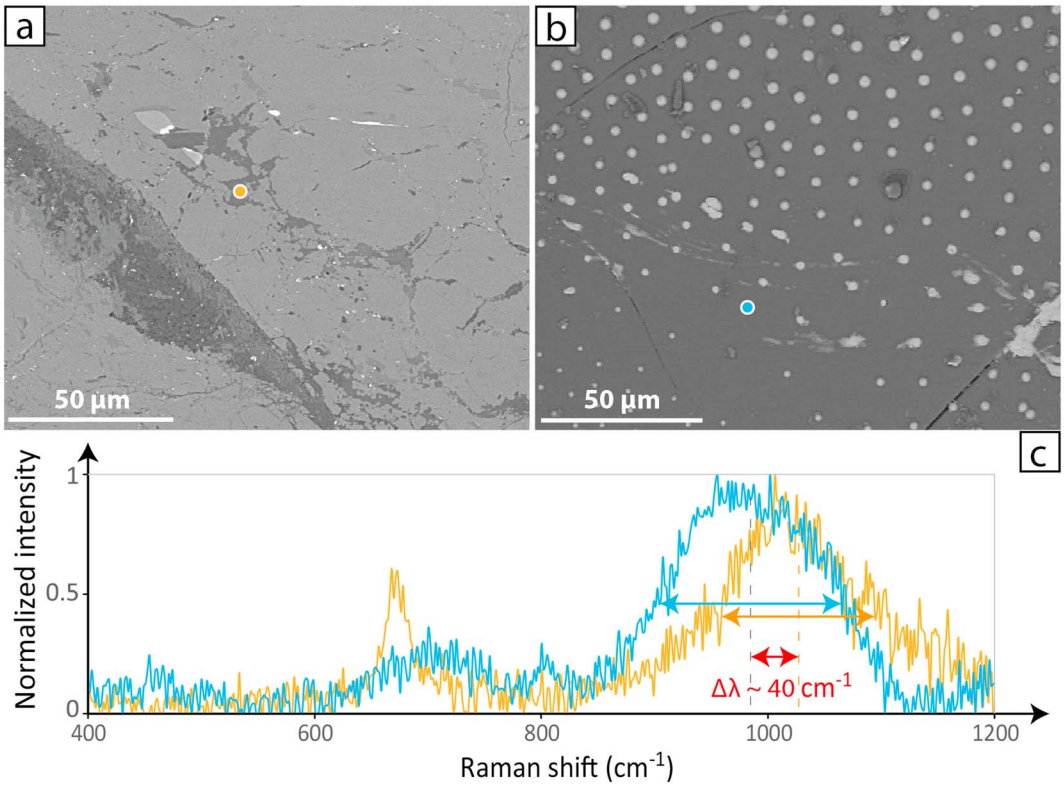

Figure 9. Raman spectra of natural and laboratory ultramafic amorphous material. (a) amorphous pocket with average peridotite composition in sample E3a, located in Figure 4; (b) experimental ultramafic glass made with a fresh Balmuccia peridotite fragment heated for 2 hr at 1450°C and atmospheric pressure; (c) Raman spectra for both natural (yellow, a) and laboratory (blue, b) amorphous materials. In the laboratory, iron oxides separated from the liquid silicate, especially leading to spherulites upon quenching. Both spectra show typical broad signal between 900 and 1,100 cm^{-1}, which corresponds to disorganized T-O-T vibrations, that is, bounds between tetrahedral sites occupied by Si^{4+}. The difference in Raman shift (red) may be due to little chemical variations and also to effects of the pressure at which the glass was formed (ambient for the laboratory, $>$ 1 GPa for the natural glass).

originate from a metamorphic reaction between the glassy "bytownite" and the host pyroxene above 1.1 GPa. Moreover, the presence of talc just next to this partially transformed injection vein and the absence of transformation in still isolated other pockets together suggest that these reactions are related to late fluid circulation.

Raman spectrometry also reveals that the glass pockets contain a significant amount of water (Figure 8d), whereas the host peridotite, where not altered, is totally dry. The water content $C_{H_2O}(\text{wt\%})$ is estimated using the following equation (Le Losq et al., 2012): $C_{H_2O}(\text{wt\%}) = 100{\cdot}A{\cdot}R_{w/s}/\left(1 + A{\cdot}R_{w/s}\right)$, where A = 0.007609 and $R_{w/s}$ is a measurement of the relative intensity contributions of glass and dissolved water in the Raman spectrum. The water content here is ≈ 1.5 wt%, mostly consisting in structurally bound OH (Figure 8e), originally present in the melt (Le Losq et al., 2012). This structurally bound OH corresponds to water which could not have been incorporated in the glass after its solidification.

3.3. Pressure-Temperature Conditions During the Pseudotachylyte Formation

The ambient temperature of the peridotite during pseudotachylyte formation was between 600 and 800°C (Souquière & Fabbri, 2010; Ueda et al., 2008). Stable Al-spinel is observed in the ultramylonite-like veins (Figures 7a and 7b). In nonaltered areas, that is, without retrograde phases, these spinel grains are euhedral, revealing that they were in equilibrium with olivine and pyroxene during their crystallization. This and the absence of plagioclase in the pseudotachylyte vein branches demonstrate that the pressure was between 1.1 and 1.5 GPa or greater (Green & Hibberson, 1970), which implies that the earthquake at the origin of the pseudotachylyte formation occurred at a depth of about 40 km or more, if pressure is considered as lithostatic during postmelting crystallization.

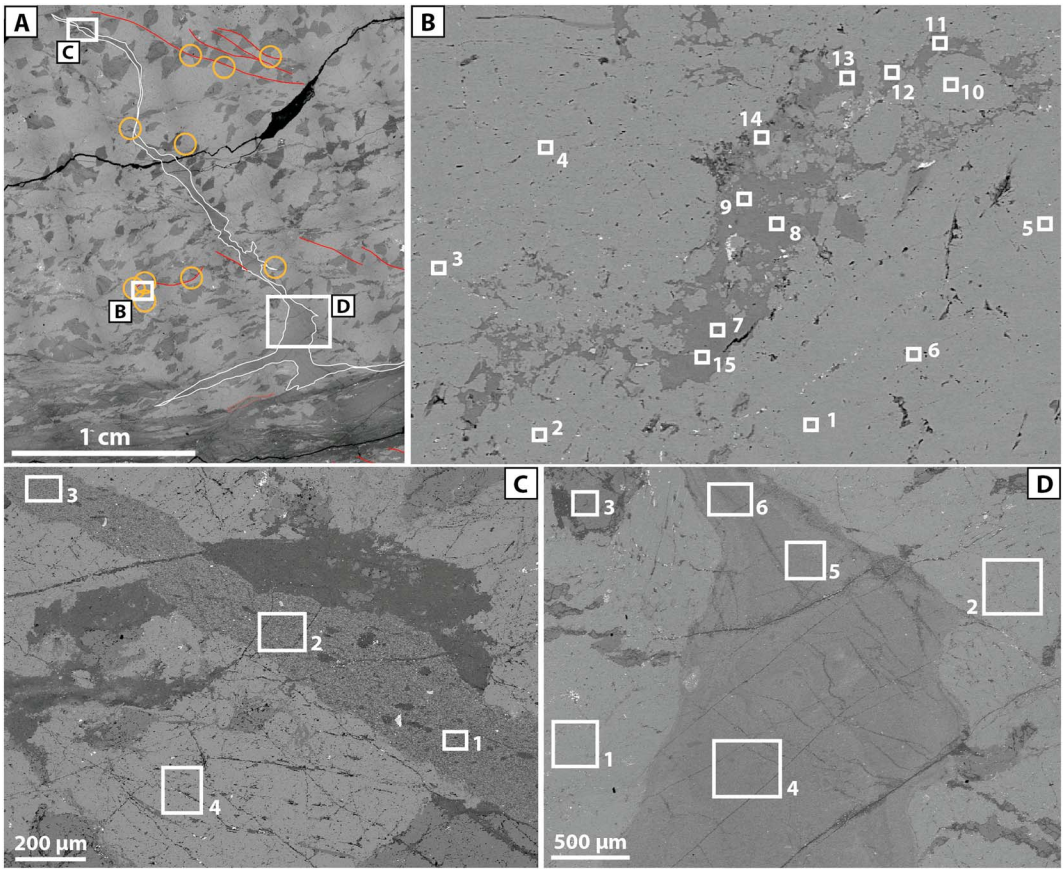

Figure 10. Chemical analysis of preserved injected material. (a) Pluricentimetric injection vein of sample E3b (Figure 4e). (b) Unaltered amorphous pocket shown in Figure 8c. (c) Tail of the injection vein. (d) Root of the injection vein. Numbers in (b), (c), and (d) indicated areas where energy dispersive X-ray spectrometry measurements were made. The energy dispersive X-ray spectrometry data are shown in Table 1.

Field observations in the Cima di Gratera region (Alpine Corsica) suggest similar pressure conditions during the Alpine metamorphism, that is, ≈ 1.3 GPa and ≈ 450°C (Lahondère & Guerrot, 1997; Vitale-Brovarone et al., 2013), but without any accurate *P-T* conditions determination (Magott et al., 2016). Pseudotachylytes of the Alpine Corsica peridotites are assumed to have formed with a maximum pressure between 1 and 1.5 GPa (e.g., Austrheim & Andersen, 2004; Deseta, Andersen, & Ashwal, 2014, Deseta, Ashwal, & Andersen, 2014). Ultramafic pseudotachylytes of similar scale (thickness and offset) were already documented in the Balmuccia peridotite (Ueda et al., 2008) and in the Lanzo peridotite (plagioclase peridotite; Piccardo et al., 2010) but at pressures lower than 800 and 500 MPa, respectively.

Overall observations confirm the results of Souquière and Fabbri (2010) and Ueda et al. (2008), even if the temperature estimate in the host rock was probably closer to 600°C than to 800°C (T. Ueda, personal communication, 2017).

3.4. Focal Mechanism Reconstruction Using Electron Backscattered Diffraction

Ultramylonite-like veins (Figures 4, 6, 7, 9a, and 12), filled with micrometric grains (0.2–2 µm) of olivine, pyroxene, and Al-spinel, exhibit limited but clear and constant fabric (< 2.5 MUD, multiples of uniform distribution, Figure 6). Olivine (010) planes are parallel to the fault plane, and [100] or [001] directions, less textured (< 1.9 MUD), could indicate the slip direction (Figure 6f); diopside and olivine [100] axes show similar orientation (Figure 6g).

The olivine fabric, with [010] axis normal to shearing and other axes faintly textured, was observed in the laboratory during shearing of partially molten peridotites (Holtzman et al., 2003). It is also consistent with high-temperature (>1250°C) diffusion-accommodated grain boundary sliding (Miyazaki et al., 2013), which

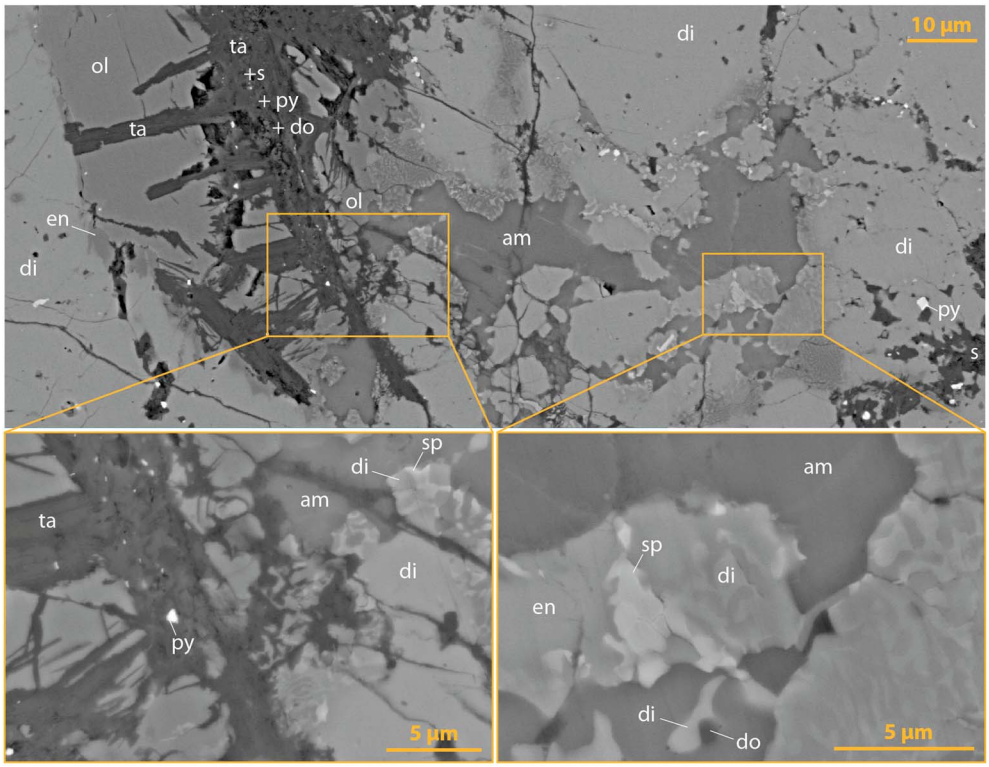

Figure 11. Amorphous pocket in a diopside grain next to a partially altered olivine grain. Spinel-diopside and spinel-enstatite symplectites have grown around the amorphous material. Sample E3b. Legend: am = amorphous; di = diopside; en = enstatite; do = dolomite; ol = olivine; py = pyrite; s = serpentine; ta = talc.

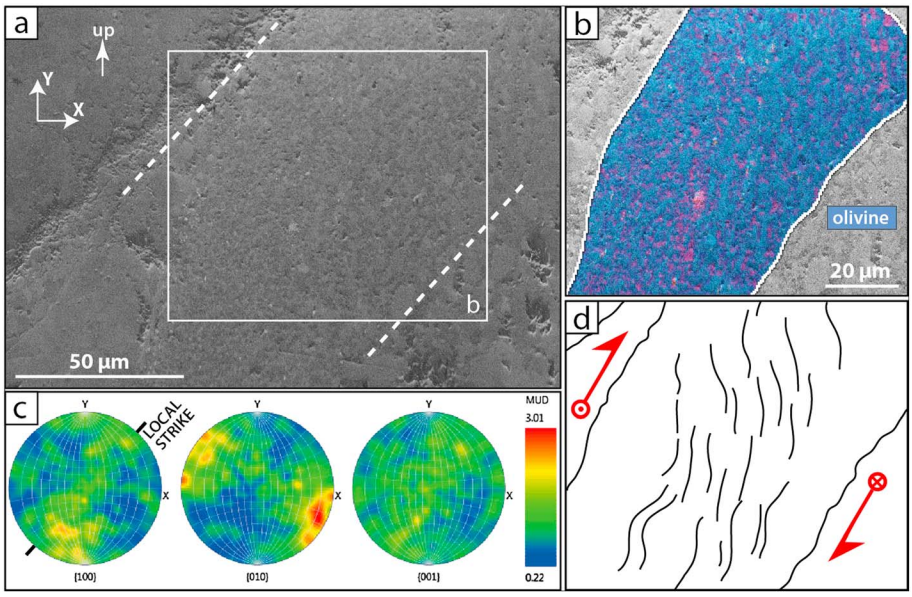

Figure 12. Vertical section revealing a relationship between CPO and shape preferred orientation in microcrystalline olivine. (a) polished surface showing micrometric grains of the fault gouge, located in Figure 4e; (b) phase map indicating olivine indexation in blue; (c) electron backscatter diffraction pole figures (in plane) showing olivine CPO consistent with results presented in Figure 6; (d) simple sketch highlighting S-C fabric and related sense of shear. The horizontal sense of shear is also indicated. In addition, olivine grains are elongated along their [100] axis. Pink color: absence of indexed olivine. Upper stereographic projection. MUD = multiples of uniform distribution. Analysis points number: 25422. Indexation: 56.88%. Olivine: 91.4%.

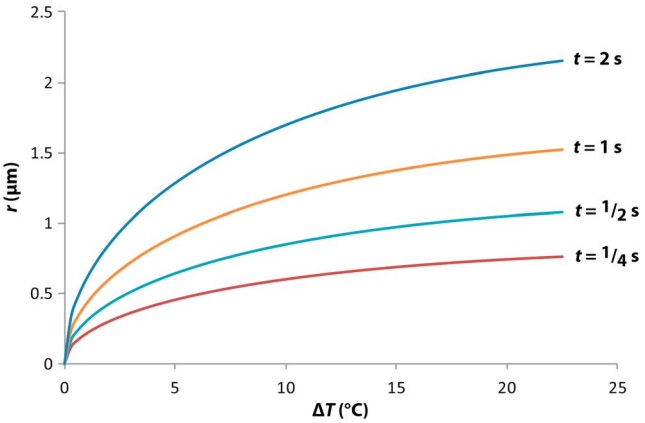

Figure 13. Microcrystalline olivine radius as a function of overcooling and time. Radius that olivine grains nucleating from the ultramafic melt can reach if they grow during t with an overcooling of ΔT. For olivine crystals to reach r= 1 µm, as seen in ultramylonite-like veins, a ΔT of a few tens of degrees is sufficient even if it lasts less than 1 s.

suggests that the vein developed at a higher temperature than what the ambient metamorphic grade implies. In addition, a vertical section (Figure 12) in the same microfault segment (Figure 4e) shows the same olivine crystal preferred orientation (CPO) with clear shape preferred orientation (SPO) and S-C fabric confirming the dip-slip component (north up, south down).

In the configuration proposed in Figure 5 the olivine and diopside [100] axes would be parallel to the slip direction; on the contrary, if the southern half-space had risen, the [001] axes would have broadly pointed out the sliding direction. High-temperature diffusion creep experiments may show either [100] or [001] axes in the slip direction. For shear experiments performed at 1200°C and 1.6 GPa, the olivine [001] axis is parallel to the shear direction (Sundberg & Cooper, 2008); at 1300°C and ambient pressure, the olivine [100] axis becomes parallel to shearing (Miyazaki et al., 2013). These CPO develop in the absence of dislocation activity (Miyazaki et al., 2013; Sundberg & Cooper, 2008). Furthermore, if the micrometric grains of the ultramylonite-like veins network crystallized from the frictional melt, an oriented crystallization should have significantly contributed to the CPO, as evidenced in near-solidus high-pressure faulting experiments (e.g., Negrini et al., 2014). In that case, [100] axes of both olivine and diopside should indicate slip direction due late coseismic creep. The olivine SPO (Figure 12) could be due to oriented crystallization, as it reveals that olivine grains have mainly grown along the [100] axis. Nevertheless, it is also consistent with melt-free solid-state deformation (Maruyama & Hiraga, 2017; Miyazaki et al., 2013).

The radius r of olivine grains crystallizing from the melt can be calculated using the following equation (Maaløe, 2011): $r = \sqrt{2Dv(c-s)t/[ae^{bv(c-s)}]}$, where D is the diffusion coefficient (10^{-7} cm^2/s; Donaldson, 1975; Hofmann, 1980), v is the molar volume (~43.67 cm^3/mol), a = 0.9277, b = 3.0754, $(c-s)$ is the supersaturation, and t is the period during which the liquid undergoes supersaturation. According to Maaløe (2011), $(c-s) = 1.5.10^{-4} \times \Delta T$, ΔT being the overcooling. Figure 13 plots the radius r that olivine grains crystallizing from the melt can reach as function of time and overcooling. Overcooling, which is consistent with fast cooling and heat loss within the fracture walls, promotes fast growth, and olivine grains can certainly reach more than 1 µm within a few seconds (Figure 13). This is consistent with the possibility that olivine crystals of the veins network may originate from the nearly instantaneous cooling of the rupture-induced melt layer. We argue that melt progressively crystallized while migrating from the fault vein into tensile fractures, resulting in Na-enriched glass quenching at the end of injection veins (Table 1).

The CPO of olivine [010] axis is stronger because its texturation begins as soon as grains nucleate in the frictional melt, which undergoes high shear strain at high temperature (>1250°C) till the beginning of late coseismic creep, that is, ~1 s after the passage of the rupture front. This high-temperature fabric is then mainly preserved by quenching. The weaker CPO of [100] and [001] axes would be due to melt-free shearing during cooling, that is, late coseismic creep. Thus, this CPO would constitute the first observed direct record of sliding and sliding direction in an ultramylonite-like vein originating from the crystallization of a pseudotachylyte.

The pole figure for the [100] direction shows an angle of ~ 40° with respect to Z axis (normal to the polished surface), which yields a dip-slip component of 1.2–1.5 m and a probable reconstructed total relative displacement of 1.6–1.9 m. Furthermore, as the horizontal component is dextral, the sliding direction observed by electron backscattered diffraction (EBSD) confirms that the northern half-space rose in relation to the southern one (Figure 5). Considering that the large injection vein indicates the dilatation quadrant, the northern half-space should have been affected by a rupture coming from above. Lastly, this focal mechanism reconstruction is not corrected of the Alpine verticalization of the Ivrea-Verbano Zone.

3.5. Pseudotachylyte Preservation and Strength Throughout Alteration

Dolomite, serpentines, sulphides, and amphiboles are only observed in the main pseudotachylyte surfaces and in late fractures associated with limited deformation and localized alteration during exhumation of the

Table 1
Chemical Analysis of Preserved Injected Material

Studied area	Spectrum	O	Na	Mg	Al	Si	K	Ca	Ti	Cr	Fe
(B)	1	60.20	0.48	8.13	2.11	19.34	0.00	8.50	0.16	0.20	0.89
	2	60.16	0.53	8.47	1.61	19.78	0.00	8.76	0.00	0.00	0.68
	3	60.17	0.49	8.25	1.95	19.55	0.00	8.68	0.00	0.14	0.77
	4	60.22	0.48	8.53	1.44	19.89	0.00	8.63	0.00	0.13	0.67
	5	60.36	0.00	8.37	1.90	19.69	0.00	8.60	0.00	0.16	0.93
	6	60.39	0.00	8.62	1.45	20.06	0.00	8.77	0.00	0.00	0.70
	7	61.71	2.21	0.00	12.72	18.17	0.00	5.19	0.00	0.00	0.00
	8	61.72	1.36	0.00	13.64	17.31	0.00	5.97	0.00	0.00	0.00
	9	61.32	1.15	3.52	11.30	17.57	0.00	4.65	0.00	0.00	0.49
	10	60.31	0.00	8.32	2.13	19.55	0.00	8.80	0.00	0.00	0.90
	11	61.68	1.82	0.00	13.24	17.66	0.00	5.60	0.00	0.00	0.00
	12	61.69	1.29	0.00	13.84	17.10	0.00	6.08	0.00	0.00	0.00
	13	61.72	1.26	0.00	13.56	17.29	0.00	6.16	0.00	0.00	0.00
	14	60.28	0.00	16.47	0.00	20.55	0.00	0.14	0.00	0.00	2.56
	15	61.55	1.77	1.00	11.81	18.07	0.00	5.80	0.00	0.00	0.00
(C)	1	61.60	0.18	10.83	1.14	19.25	0.00	5.71	0.00	0.15	1.13
	2	61.74	0.17	10.95	1.29	19.03	0.11	5.35	0.00	0.15	1.22
	3	60.71	0.21	9.93	1.09	19.91	0.00	6.68	0.00	0.17	1.30
	4	60.39	0.51	7.90	2.60	19.28	0.00	8.34	0.12	0.00	0.86
(D)	1	59.98	0.47	8.35	1.62	19.61	0.00	8.63	0.09	0.30	0.96
	2	60.84	0.44	8.59	1.60	19.29	0.00	8.11	0.00	0.27	0.87
	3	59.64	0.00	16.49	1.14	19.99	0.00	0.15	0.00	0.13	2.46
	4	59.88	0.00	15.66	1.28	17.79	0.00	3.37	0.00	0.17	1.86
	5	60.34	0.00	14.93	1.37	18.04	0.00	3.41	0.00	0.15	1.75
	6	60.32	0.00	15.02	1.36	18.07	0.00	3.23	0.00	0.15	1.84

Note. Energy dispersive X-ray spectrometry data, performed in sample E3b. Studied areas are located in Figure 10 and entire sample in Figure 4e. Red and green colors are used for data respectively corresponding to fully crystalline and fully amorphous material. Data are atoms proportions. Sodium is not present in the fully crystalline pluricentimetric injection vein (D4–6) as well as in host rock enstatite (D3), very low in host rock diopside (D1–2, C4, B1–6, and B10), and substantially higher within the amorphous material. Within the tail of the injection vein (C), Sodium is low but present (C1–3), suggesting either amorphous material or higher ionic diversity in minerals due to fractionated crystallization. Data are semiquantitative.

Balmuccia massif. In addition, apatite is abundant in the large injection vein (sample E2, located in Figure 3), which is highly altered and constituted a weakness plane during the Alpine collision. Alteration also affects the main sliding surfaces, micrometric crystals (and/or glassy material) of the millimetric fault cores being transformed into hydrous phases as talc, chlorite, and serpentines.

Thin pseudotachylyte branches, that is, ultramafic ultramylonite-like veins, are also locally affected by alteration, as well as a few millimetric amorphous injections. As an overall observation, the thicker and the more connected the pseudotachylyte branches, the lower their preservation. While at sample scale the main slip surfaces seem more altered than the damage zone (fault and injection veins), at outcrop scale, large injection veins seem much more altered and show shearing associated with low-grade metamorphism (Souquière & Fabbri, 2010). Most likely, a population of large injection veins, weaker than thin fault veins, have permitted, by coalescence, the exhumation of undeformed pseudotachylyte segments, like the one studied here.

The concept of pseudotachylyte preservation is strongly related to the possibility that pseudotachylytes are transformed into high-strain ultramylonites, as supported by many studies (e.g., Menegon et al., 2017; Pennacchioni & Cesare, 1997; Ueda et al., 2008; White, 1996). Nevertheless, these observations are in good agreement with several publications highlighting the high strength of faults that are welded by pseudotachylytes (Di Toro & Pennacchioni, 2005; Mitchell et al., 2016; Proctor & Lockner, 2016).

4. Discussion

4.1. Energy Balance

4.1.1. Thermally Dissipated Energy: Melting as Main Dissipation Process

The thermally dissipated energy Q_f is estimated from melt volume, which is mostly injected in tensile fractures (green on Figure 3). It can be calculated as a function of the molten zone thickness w (Figure 4),

Table 2
Molten Zone Thickness as a Key Parameter

w (mm)	Q_f (MJ/m^2)	τ (MPa)	$\bar{f}$	ΔS (m^2)	$t_{\Delta S}$ (s)
1	5	5	5×10^{-3}	≈ 10, 000	~10
10	50	50	5×10^{-2}	≈ 1, 000	~1
100	500	500	5×10^{-1}	≈ 100	~0.1

Note. Energy dissipated by melting Q_f, shear strength τ, effective friction $\bar{f} = \tau / P_c$, drainage area ΔS, and time $t_{\Delta S}$ as a function of the molten zone thickness w. Drainage area ΔS is the fraction of the fault from which the melt is able to be sucked out due to the opening of a tensile fracture. The time $t_{\Delta S}$ is calculated for a dynamic friction coefficient $f_d = 10^{-3}$.

as follows: $Q_f = \rho \cdot [H + C_p \cdot \Delta T] \cdot w$ (Di Toro et al., 2006), where $H = 0.3$ MJ/K (latent heat of fusion), $\rho = 3.3$ g/cm^3 (density), $C_p = 1$ kJ·kg^{-1}·K^{-1} (heat capacity), and $\Delta T = 1000$–1200 K. Thus, if $w = 1$ cm, Q_f is about 5. 10^7 J/m^2. The thickness w is not the current thickness of the pseudotachylyte but the thickness of the effective molten zone which lubricated sliding before injection. The plurimetric injection vein (Figure 3) consists of ≈ 15 m^3 of altered glass (>80%) and clasts (<20%), which is consistent with previous observations on the Lanzo peridotite (Piccardo et al., 2010) and in Alpine Corsica (e.g., Andersen et al., 2014). The required energy to melt $V_{inj} = 12$ m^3 of peridotite is $Q_{inj} = \rho \cdot [H + C_p \cdot \Delta T] \cdot V_{inj} \simeq 50$ GJ. This energy Q_{inj} is the energy dissipated by melting on a limited fraction of the fault surface. The volume V_{inj} contains the melting product corresponding to a fraction ΔS, that is, drainage area, with $\Delta S = Q_{inj}/Q_f = V_{inj}/w$. Different values of w can thus be tested (Table 2) to check their consistency.

4.1.2. Fracture Surface Energy: Estimates and Limitations

Mitchell and Faulkner (2009) described two end-members in fault structure: (1) one fault core with a narrow damage zone or (2) a multiple fault core with highly damaged rock lenses and a strain exponential decay around the main slip surfaces. The studied fault segments are thinner and exhibit an intermediate morphology between these two end-members.

For a ≈ 6 cm long fault segment (brown on sample E3a, Figure 4d), the minimum cumulative length of the microfaults and microfractures network, estimated from effective length of visible cracks and offset grains for healed cracks, is ≈ 45 cm for a 15-cm^2 surface (southern half of sample E3a). By symmetry, and taking into account the second fault segment (branch 2, Figure 3), this cumulative length reaches ≈ 200 cm. Moreover, the northern half-space seems at least twice as fractured as the southern part. This asymmetry reflects the asymmetric dynamic stress field associated with the rupture propagation (Di Toro et al., 2005), and suggests, along with the plurimetric injection vein, that the northern half-space corresponds to one of the fossilized dilatation quadrant. The cumulative length of microfractures possibly reaches ≈ 500 cm. Considering that our observations can be extrapolated to the third dimension, we can calculate, at first order, the ratio between the real fracturing surface and the apparent fault surface $R_1 = (500/6)^2 \sim 7,000$ (i.e., square meters of fractures in the damage zone divided by square meters of macroscopic fault). Even if we thereafter demonstrate that the ultramylonite-like veins are crystallized pseudotachylytes, an alternative calculation could consider grain size reduction (Brantut et al., 2008) between the beginning and the end of the dynamic event: $R_2 \sim 6w/d$, where w is the gouge thickness (here the cumulative thickness of the fault network) and d the grain diameter in the aggregate. As $R_2 \sim 6 \times 10^{-2}/10^{-6} = 6 \times 10^4$, most of the surface energy in the fault would be held by grain boundaries.

During rupture propagation ($v_r \approx 5$ km/s; Madariaga, 1977) and the sliding caused by it ($v_{sl} = 1$–10 m/s), part of the elastic energy is released by fracturing. The fracture surface energy per surface unit can be estimated using the product of olivine fracture energy ($\gamma \sim 0.5$ J/m^2 at 500–800°C, e.g., Darot et al., 1985) and surface ratio R ($<7 \times 10^4$) as follows: $G = \gamma \cdot R < 10^5$ J/m^2, which is negligible compared to Q_f, as already observed for other pseudotachylytes (e.g., Pittarello et al., 2012).

Nonetheless, this value of G does obviously not inform about the entire fracturing, as part of it is included in Q_f, melting being necessarily preceded by fracturing. In other terms, the separation of G and Q_f is not fully physically correct. Besides, according to seismological studies, fracture energy G can be estimated as a function of sliding D (Abercrombie & Rice, 2005). For intermediate earthquakes (Prieto et al., 2013), the relation is $\log G = 1,85 \log D + 8$. For $D = 1$ m, G would be ~10^8 J/m^2, which is above our estimate of Q_f. In seismology, Q_f is not directly measurable; however, the fracture energy G can be estimated. Recently, Passelègue et al. (2016) showed that the seismological estimates of G accounted partially for a measurement of Q_f, rather than G uniquely, because frictional weakening is essentially a thermal process (Di Toro et al., 2011). This paradox highlights that understanding pseudotachylyte generation is a key issue for earthquake energy balance.

4.1.3. Stress Drop, Seismic Efficiency, and Thickness of the Molten Zone

Because of a total displacement $D = 1$–2 m, we can reasonably argue that the magnitude of the earthquake which generated this pseudotachylyte was $6 < M_w < 7$. Considering that $M_0 = \mu \cdot D \cdot L^2$, and

Table 3
Estimate of the Earthquake Magnitude

M_w	M_0 (N·m)	L (km)	S (km^2)	$\Delta\tau_{sismo}$ (MPa)
6	$\approx 1 \times 10^{18}$	≈ 3.7	≈ 10	≈ 65
6.5	$\approx 7 \times 10^{18}$	≈ 8.7	≈ 59	≈ 28
7	$\approx 4 \times 10^{19}$	≈ 20.5	≈ 330	≈ 12

Note. Potential magnitudes and corresponding moment, first-order fault dimensions, and stress drop. In this calculation, we assume that D = 1.5 m, $S = \pi \cdot L^2/4$, and $\Delta\tau_{sismo} = \mu \cdot D/L$.

M_w = 2/3 logM_0 − 6.07, the average length of the seismic fault should be $3 < L < 21$ km (assuming a shear modulus μ = 80 GPa). The seismological stress drop is $\Delta\tau_{sismo} = C \cdot \mu \cdot D/L$ (Kanamori, 1977), where $C \approx 1$ (geometrical parameter). Values of stress drop $\Delta\tau_{sismo}$ range between 12 and 65 MPa (Table 3), which is consistent with recent compilations (e.g., Kanamori & Brodsky, 2004; Prieto et al., 2013).

The total mechanical energy per surface unit is $E_{tot} = \bar{\tau} \cdot D$, where $\bar{\tau}$ is the average shear stress on the fault plane during the complete slip event, that is, from rupture to sliding arrest. Neglecting G, the radiative efficiency is $\eta = E_R/E_{tot} \approx 1 - Q_f/E_{tot}$. Recalling the formulation of Q_f above leads to the following relation between $\bar{\tau}$ and w (Figure 14a):

$$\bar{\tau} = \frac{\rho \cdot \left[H + C_p \cdot \Delta T\right] \cdot w}{(1-\eta)D}.$$

4.2. Sliding History

Energy balance, field observations, and EBSD measurements are consistent with a dextral sense of shear with a dip-slip component of 1.2–1.5 m, that is, a probable total relative displacement of 1.6–1.9 m. This scenario (Figure 5) is also compatible with the orientation of injection veins (Figure 3), assuming sliding subparallel to rupture propagation. We still have to understand how and for how long slip occurred. The evolution of the friction coefficient during the seismic event is shown in Figure 14b and is detailed in the following subsections, in good agreement with previous work (e.g., Andersen et al., 2008).

4.2.1. Melt Viscosity and Melt Shearing

The viscosity of liquid komatiites and peridotites between 1 and 3 GPa equals that of liquid diopside (Liebske et al., 2005; Suzuki et al., 2001), which, assuming peak temperature of 1600–1800°C during sliding, is ~1 Pa·s (Taniguchi, 1992). Limited H_2O in the melt lowers the viscosity down to 1 order of magnitude (Vetere et al., 2006), which would lead for a peridotitic melt to a viscosity of ~0.1 Pa·s. As probably 0.1 to 1 wt% of H_2O is present in the melt, the viscosity v_0 was $<10^{-1}$ Pa·s. Such a low viscosity is consistent with field observations of pseudotachylytes in Alpine Corsica (Andersen et al., 2014). According to the Einstein-Roscoe equation (e.g., Pinkerton & Stevenson, 1992), the average mush viscosity (melt + crystals) v is related to the liquid viscosity v_0 and the clasts fraction ϕ as follows:

$$v = v_0(1 - \kappa \cdot \phi)^{-n},$$

with $\kappa \approx 1.21$ and $n = 2.5$. Observations lead to ϕ = 10–20%, and assuming v_0 = 0.1 Pa·s, the melt viscosity was of the order v = 0.16 Pa·s. Note that only crystals fractions above $\phi > 40\%$ may lead to an average mush viscosity $v > 1$ Pa·s.

Assuming a Newtonian fluid, τ_{ss} is directly related to the viscosity v, as follows: $\tau_{ss} = v \cdot \dot{\gamma}$, with the strain rate $\dot{\gamma} = v_{sl}/w$. Assuming v = 1 Pa·s and a typical seismic strain rate $\dot{\gamma} = 10^3$-10^6 s^{-1} leads to a steady-state shear stress τ_{ss} of the order of a few kilopascals to a few megapascals only. This is consistent with recent numerical results (Platt et al., 2014) which showed that assuming that all the strain was localized in the silicate melt, a shear stress of ~10 MPa during melt-assisted sliding implies that strain is localized on a layer thinner than 1 μm for $v_{sl} > 10$ m/s, that is, ultralocalization. This also implies that the dynamic stress drop was total, at least transiently, during high-velocity sliding.

Finally, using the estimates of $\Delta\tau_{sismo}$ as a function of M_w, the upper bound for average shear stress for the whole sliding event is $\bar{\tau}_{max} = \tau_{ss} + \Delta\tau_{sismo} \sim \Delta\tau_{sismo}$. Values of $\bar{\tau}_{max}$ for M_w 6 and M_w 7 earthquakes are plotted (Figure 14a). Field observations ($w > 5$ mm) are incompatible with a M_w 7 earthquake, even for a very low radiative efficiency. For a M_w 6 earthquake, $\Delta\tau_{sismo}$ is compatible with w for radiative efficiencies typical of intermediate and deep earthquakes ($0.1 < \eta < 0.5$; Kanamori & Brodsky, 2004; Prieto et al., 2013). Finally, the friction coefficient appears to range over several orders of magnitude. Indeed, recalling the normal stress to be greater than 1 GPa (40 km depth), we find an effective friction coefficient of 3 or 4×10^{-2}, that is, averaged on the entire event. Again, this implies that the dynamic stress drop was complete, at least transiently, during high velocity sliding.

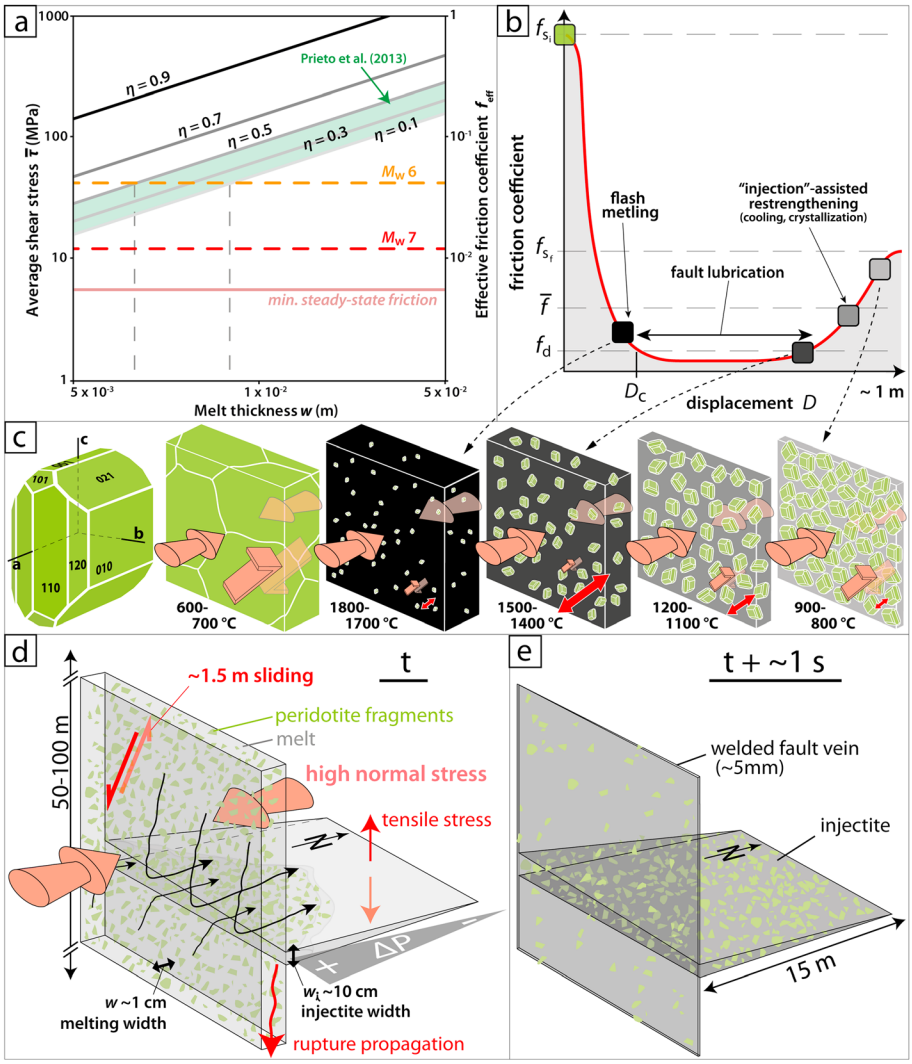

Figure 14. Energy balance and sliding history. (a) Average shear stress and effective friction as a function of molten zone thickness, showing that the earthquake magnitude is between 6 and 6.5 for a radiative efficiency $0.1 < \eta < 0.5$. b: Friction coefficient evolution during sliding. The dynamic friction coefficient f_d is defined as $\tau_{ss} = f_d \cdot \sigma_n$. Maximum value of average friction coefficient is defined as $\bar{\tau}_{max} = \bar{f}_{max} \cdot \sigma_n$. Static friction coefficient f_s is assumed lower after fault formation. Squares refer to illustrated steps (c). (c) Sketch of an olivine crystal (modified after Deer et al., 1992) and summary of the physical evolution of a representative elementary volume (100 μm^3, no clast) undergoing total melting on the rupture path. Olivine crystals nucleate from the melt and develop a CPO as described in text. Red arrows indicate, from top to bottom, normal stress, shear stress, and sliding directions; different sizes illustrate the evolution of those parameters during lubrication and restrengthening, in correlation with (b). (d, e) Diagram depicting the relationship between the fault and the injection vein. The sliding history is deduced from geometrical constraints along with electron backscatter diffraction measurements and is consistent with the energy balance described in text. Present-day pseudotachylyte (e) is here assumed to have kept the geometry frozen from t + 1–10 s, with t being the earthquake time.

This study suggests that melt-assisted sliding during local but total fault lubrication may constitute the deformation mode in the upper mantle. The minimal shear stress, that is, steady-state shear stress τ_{ss} during fault lubrication, can be extrapolated from Nielsen et al. (2008), leading to $\tau_{ss} \propto \sigma_n^{1/4}$, that is, $\tau_{ss} \approx 5$ MPa for $\sigma_n \approx P = 1$ GPa. As τ_{ss} does not vary much with σ_n, this estimation can be considered as relatively robust. Such low shear stress values mean that melt-assisted sliding can be predicted by calculation.

4.2.2. Sliding-Induced Crystallographic and Shape Preferred Orientations

A summary of the physical evolution of a representative elementary volume of peridotite undergoing total melting on the rupture path is shown in Figure 14c. The representative elementary volume is about ~100 μm^3 and does not include clasts. Olivine crystals nucleate from the melt and develop a CPO in two steps.

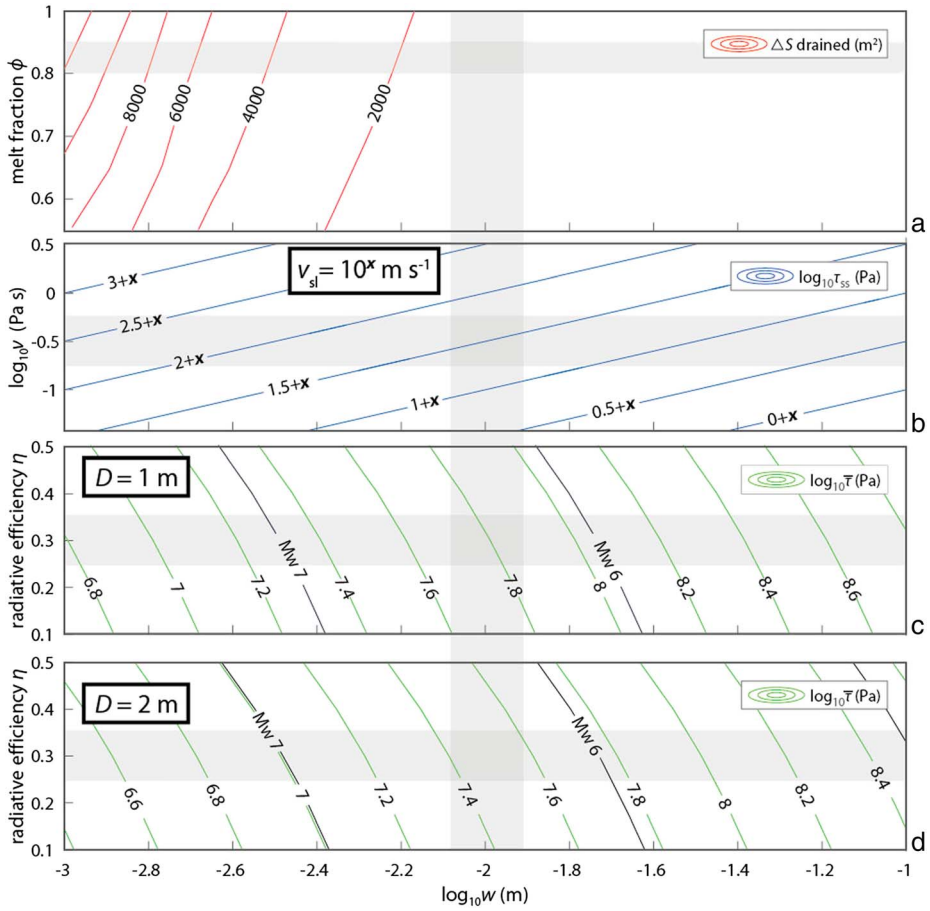

Figure 15. Dynamic sliding parameters and variables during melt-assisted sliding as a function of the thickness of the effective molten zone. (a) melt fraction ϕ and associated drainage area ΔS of the outcrop-scale injection vein; (b) effective melt (liquid + clasts) viscosity ν and associated steady-state shear stress τ_{ss} during fault lubrication for a given sliding velocity v_{sl}; (c, d) radiative efficiency η and associated average shear stress $\bar{\tau}$ during the whole sliding event with D = 1 m (c) and D = 2 m (d), showing relative consistency with magnitude estimate.

First, above 1300°C, due to high normal stress and low viscosity, the [010] axis becomes oriented normal to the fault. Then, due to melt suction, fast cooling occurs ($<$ 1 s), which slows crystal growth down. Residual melt percolates to the tip of "injection" veins, leaving well-sintered aggregates of submicrometric crystals and residual amorphous material in the fault vein. Finally, below 1200°C, limited solid-state deformation occurs during the last stage of restrengthening, referred to as late coseismic creep. In addition, the weak SPO seems to correlate with the CPO, with an elongation of olivine [100] axis in the sliding/flow direction, which would be consistent with the above mentioned melt-free deformation (Maruyama & Hiraga, 2017; Miyazaki et al., 2013).

4.2.3. Earthquake Dynamics, Melt Injection, and Slip Hardening

Using previous calculations, the dynamic shear resistance $\tau_f = Q_f/D$ is about 5–500 MPa (Table 2) and the average friction coefficient $\bar{f}$ is about 10^{-1}. Besides, the dynamic friction coefficient $f_d = \nu \cdot \dot{\gamma}/\sigma_n$, with $\dot{\gamma}$ the strain rate in the molten zone, is ~ 10^{-3} if $\dot{\gamma} = 10^6$ s^{-1}, that is, ultralocalization and total lubrication. As illustrated in Figure 15, for reasonable values of melt effective thickness w, melt fraction ϕ, effective viscosity ν, sliding velocity v_{sl}, and radiative efficiency η, we obtain consistent estimates for the drainage extent ΔS (Figure 15a), the shear stress during lubrication τ_{ss} (Figure 15b) and during the whole slip event $\bar{\tau}$ (Figures 15c and 15d). Stress and seismic efficiency expectations are in good agreement with magnitude estimates (Figures 15c and 15d).

The planar geometry of the plurimetric injection vein strongly suggests that it is a tension crack, which opened normal to σ_3 when the rupture front passed. To know how the melt was transported from the

melting area (fault plane) to ~15 m inside the dilatation quadrant (Figures 14d and 14e), we calculate the Reynolds number $R_e = \rho \cdot v_{inj} \cdot w_i/\nu$, with v_{inj} (injection velocity), $w_i \sim 10$ cm (the tensile crack effective opening). Assuming $v_{inj} = 1$ m/s and $\nu = 1$ Pa·s, then $R_e \sim 100$, which means that the flow is laminar and the Poiseuille's equation is applicable (Figures 14d and 14e)

$$v_{max} = {w_i}^2/(8{\cdot}\nu){\cdot}\Delta P/\Delta x$$

Assuming a drop of only 10% of the pressure in tensile fractures due to rupture propagation ($\Delta P \sim 100$ MPa), and knowing the penetration length $\Delta x \approx 15$ m, then $v_{max} \approx 2$–10 m/s. This means that a 10% drop is sufficient for the Poiseuille maximum velocity to overtake, at least locally, the sliding velocity. Thus, transient pressure drop in tensile fractures may drive melt suction out from the fault plane (Nielsen et al., 2010; Sibson, 1975), which would lead to rapid cooling and solidification. Thinning of the melt layer would lead to an increase in strain velocity, which may participate in hardening and inhibit slip.

Finally, with $v_{max} \approx 10$ m/s, the suction effect would be able to drain ≈ 100 m^2 on the fault surface in less than 1 s in the vicinity of the fracture, that is, in a comparable duration than sliding and melting, which is compatible with $w \sim 1$ cm (Table 2).

The [100]-axis texture, interpreted as parallel to flow for both olivine and diopside, is likely to originate from the minimization of crystallization energy during cooling. Both transient complete fault lubrication (Di Toro et al., 2011) and high normal stress ($>$ 1 GPa) are consistent with the activation of the (010) [100] slip system during melt crystallization and the consecutive slip slowdown.

4.3. Pseudotachylyte Preservation and Interplay With Mylonitic Shear Zones

4.3.1. Welding and Pseudotachylyte Strength

The welding process may depend on the temperature evolution during strain localization and on sucking efficiency of tensile fractures, both controlling the final thickness of fault veins. The difference in temperature between the host rock and the melting point differs from other records in mantle or crustal outcrops, probably influencing the time and space scales of the process zone behind the rupture propagation front. Heating and cooling rates may also control crystal growth (e.g., Maaløe, 2011) and clast fraction. Crystallization velocity depends on the melt chemistry, as chemistry impacts viscosity (e.g., Suzuki et al., 2001). Fault reactivation may thus be prevented by an efficient welding, that is, a very thin fault vein (~1 mm), with a low fraction of clasts and gouge (crystallized melt) patches, which would decrease shear strength. As a consequence, the preservation of the pseudotachylyte record may depend on the depth and thermal regime in the rock body in which the earthquake occurs. In other terms, pseudotachylyte generation may be more common than imagined, because most of the time the record is destroyed by various alteration processes (Kirkpatrick & Rowe, 2013) before it reaches the surface.

4.3.2. Melt-Derived Ultramylonite-Like Veins as Parts of the Preserved Pseudotachylyte

High-temperature ultramylonites formed in the spinel lherzolite facies, around 800°C (Ueda et al., 2008), but these structures do not inform about their entire formation. The mylonitization can be a long-term process due to strain localization in a solid rock volume (e.g., Trouw et al., 2009) but also a fast process occurring after the crystallization of the frictional melt at high pressure and varying temperature, that is, postseismic creep (Druiventak et al., 2012; Küster & Stöckhert, 1999), here referred to as late coseismic creep. In most cases, the mylonitization is able to erase the pseudotachylyte microstructure, leaving sharply bound ultramylonitic bands.

High-speed slip experiments show that comminution and frictional melting are coeval and not mutually exclusive processes (Spray, 1995, Passelègue et al., 2016a) at moderate slip velocities. Furthermore, experimental deformation of cataclastic gouges at low strain rate, that is, 8 orders of magnitude lower that those causing earthquakes, show amorphous material associated with fine to ultrafine grains (Peč et al., 2012), which may question both about the production mechanism of the melt and about the scale at which weakening and softening processes occur. Here nonetheless, outcrop-scale injection veins, together with calculations, demonstrate that the pseudotachylyte, that is, the whole network of ultramylonite-like and injection veins, is the fossilized trace of an earthquake.

The well-preserved ultramylonite-like veins described in the damaged zone around principal slip surfaces are similar to the ones associated with large strike-slip faults affecting the continental crust, that is, confining

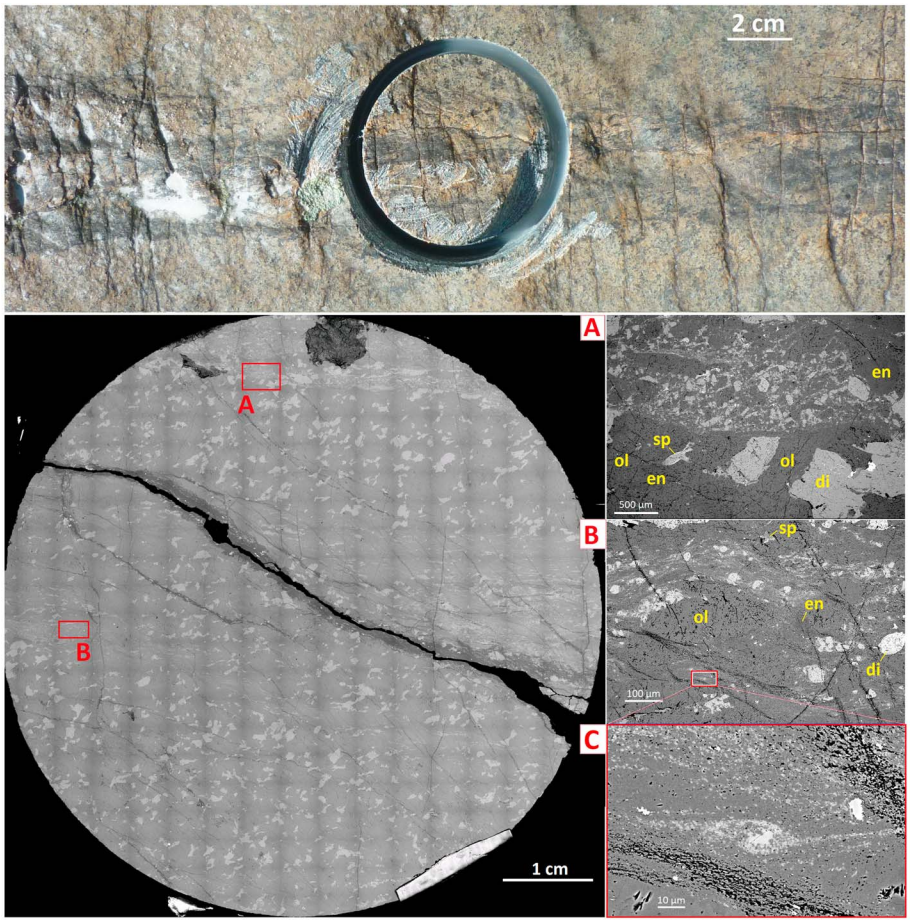

Figure 16. Closer view on a horsetail termination. Observations of sample E1, located at a horsetail termination of the fault system (Figure 3). Scanning electron microscopy (four bottom images) shows that each "hair" corresponds to a shear zone about 50 to 200 µm thick and various deformation styles depending on the distance from those shear zones. Both cataclastic (a) and mylonitic (b, c) deformation are noticed, although they formed in the same time in the same fault system. North direction is upward.

pressure ≪1 GPa, where they show semibrittle deformation down the seismogenic zone (e.g., Chester et al., 2004). Here the damage zone is quite narrow and exhibits a dense network of thin connected ultramylonite-like veins, and principal slip surfaces display mylonitic textures, evolving to cataclasites at horsetail terminations (sample E1; Figure 16), that is, where the offset tends to 0. Melting seems to have occurred where black traces are visible (e.g., Figure 16), as well as in the ultramylonite-like veins network in the damage zone. These veins are actually the consequence of the crystallization of the melt ending with late coseismic creep and could, to a certain extent, be referred to as viscously strained pseudotachylyte branches. The absence of overall significance in crosscutting relationships in the fault and injection veins network strongly suggests that they record only one seismic event. Hence, here ultramylonite-like veins formation and pseudotachylyte generation have the same origin. Actually, the ultramylonite-like veins described in this study are, along with amorphous injections, the preserved parts of the pseudotachylyte itself.

Similar ultramylonitic fault veins have been described in Corsica and are not associated with well-developed mylonite zones (Deseta, Ashwal, & Andersen, 2014), contrary to observations in other studied area (e.g., John et al., 2009) supporting contemporaneous shear-induced melting and ductile deformation. Here we show that the ultramylonite-like veins do not derive from repeated fault cycles but that they are branches of the only one pseudotachylyte, generated by a unique single seismic rupture.

4.3.3. Localized Shear Before and After Seismic Rupture

The main pseudotachylyte planes locally show mylonitized material cut by injection veins (dark blue on sample E3a, Figure 4d), revealing preseismic deformation. This shear localization may be associated with viscous heating (Braeck & Podladchikov, 2007; John et al., 2009; Kameyama et al., 1999; Kelemen & Hirth,

2007; Ogawa, 1987) just before sliding acceleration and the pseudotachylyte generation, as part of a migrating dynamic process, that is, the rupture propagation. In the periphery of such rupture surfaces, traces of viscous heating may be preserved. Strain localization might also predate the rupture nucleation, that is, an older and disconnected mylonitization event. Such possible initial precursor of shear localization, drastically oblique to the inherent planar anisotropy of the Balmuccia peridotite, might itself have been produced by an early brittle deformation event, as often evidenced in the dedicated literature (Pennacchioni & Mancktelow, 2007, and references therein). This precursor could actually be any planar heterogeneity and could be as short as some tens of meters and thinner than 10 cm. Nonetheless, while the rupture nucleation needs a precursor, the rupture propagation does not. At the scale of the studied outcrop, we do not have access to the nucleation patch.

One could imagine that postseismic slip, that is, viscous flow during later aseismic events, is recorded in the main pseudotachylyte surfaces, which are mylonitized, like the horsetail ending branch (sample E1 located in Figure 3 and shown in Figure 16) and unlikely the thin fault network (Figures 4d and 4e). However, this limited mylonitization seems to have occurred on all ending branches, which suggests that it is only associated with the end of the sliding during cooling of the newly formed grains. Moreover, the ultramylonite-like veins are not remylonitized (neither flow nor rotation features) and seems fossilized since the end of the "coseismic" sliding, that is, late coseismic creep. The temperature of 800°C (Ueda et al., 2008) associated with this preseismic and/or postseismic deformation may be 100–200°C higher than the host rock temperature.

Furthermore, as the amorphous material embedded in damaged diopside crystals contains a significant amount of water, it should undergo devitrification with time if the host rock temperature is $\geq$ 800°C. Larger melt injections have recently been described in the Lanzo massif, revealing dry glass in a dry gabbro (Scambelluri et al., 2017). Thus, the fact that glass has been preserved is also consistent with a host rock temperature of 600°C or lower during the earthquake and colder afterward.

4.4. The Roles of Water in Intermediate-Depth Mantle Earthquakes

As already suggested by experiments (Del Gaudio et al., 2009; Di Toro et al., 2006; Hirose & Shimamoto, 2005a, b), theoretical considerations (John et al., 2009; Kelemen & Hirth, 2007), and field observations (Andersen & Austrheim, 2006; Deseta, Ashwal, & Andersen, 2014), pseudotachylyte generation itself may be a deformation mode in peridotite at upper mantle conditions if the stress field is perturbed enough, especially due to mineral transformations, for example, antigorite dehydration (Ferrand et al., 2017).

Parameters controlling shear localization and thermal runaway processes are the subject of several questions. Models of these processes allow to have some idea about the mechanism of this localization (e.g., Braeck & Podladchikov, 2007; Kelemen & Hirth, 2007) but without presuming about what could promote this localization. Thermal runaway was proposed to constitute the process of pseudotachylyte generation at high pressure, but field evidence is not certain (Deseta, Ashwal, & Andersen, 2014). Here we wonder whether water, which was present, in one way or another, when the earthquake occurred, could play a role in the rupture nucleation and/or propagation.

Water influences the viscosity of silicate melts, as well as melting temperature and crystallization kinetics. Shear resistance to sliding, which may influence rupture propagation and injection veins opening, also drops with limited water amounts. As a consequence, water seems to facilitate extreme shear localization and pseudotachylyte generation. Dehydration of hydrous phases often appears to be a consequence of shear heating (Xia, 2013; Brantut, Han, et al., 2011; Brantut et al., 2008), suggesting that fluids would be a secondary factor. However, abundance of water-rich minerals exerts a strong rheological control during high strain rate deformation, facilitating thermally triggered shear instabilities (Brantut, Sulem, & Schubnel, 2011; Deseta, Ashwal, & Andersen, 2014; Yamashita & Schubnel, 2016). According to our observations, even if seismic rupture could be facilitated by thermal runaway, we still do not know anything about its actual trigger.

The relationship between intermediate-depth seismicity and hydrous minerals is still a matter of debate (Deseta, Ashwal, & Andersen, 2014; Hacker et al., 2003; Incel et al., 2017; Gasc et al., 2017; Okazaki & Hirth, 2016; Peacock, 2001). Recent experimental results show that the dehydration of antigorite even in small amounts can induce the formation of micropseudotachylytes in olivine aggregates (Ferrand et al., 2017), associated with stress drops on the order of 100 MPa and water-bearing glass in fractured olivine. A recent field study evidences high differential stress accumulated in dry and strong metabasic rocks as a trigger

for intermediate-depth earthquakes in subduction zone (Scambelluri et al., 2017), which paradoxically supports the model of Dehydration-Driven Stress Transfer (Ferrand et al., 2017). Thus, finding water fossilized in a frozen mantle earthquake, even in small amounts, suggests that hydrous minerals were present somewhere on the fault path and brings into light their possible involvement in the mechanics of earthquakes.

5. Conclusions

The studied ultramafic pseudotachylyte formed in the mantle, above 1.3 ± 0.2 GPa (42 ± 8 km depth), before tectonic emplacement of the Balmuccia slice in the lower continental crust (285 ± 15 Ma). Total melting occurred on the fault plane, transiently lubricated by a centimetric molten layer. Arguably, the pseudotachylyte is at least twice thinner than the effective molten zone at the time of the earthquake, which transiently developed during sliding migration. Hence, main pseudotachylyte fault veins are 2 orders of magnitude thinner than the total damage zone. The latter mainly consists of a network of microfaults, that is, ultramylonite-like veins, surrounded with water-bearing amorphous pockets. The ultramylonite-like veins directly originate from partial crystallization of the rupture-induced melt and record in their CPO the coseismic slip, giving access to the focal mechanism of the earthquake.

This study suggests that the pseudotachylyte segment is a piece of M_w 6–6.5 earthquake, which brings reasonable shear stress values of 10–70 MPa and an average friction coefficient of 3 or 4 × 10^{-2}. Considering a metric displacement, an average melting width of ~1 cm and a high normal stress (> 1 GPa), this yields a dynamic friction coefficient ≪0.1, consistent with complete fault lubrication. We argue, however, that the lubrication is transient, as the melt could rapidly flow (2–10 m/s) into tensile fractures, which dynamically opened in the dilatation quadrant due to rupture propagation. Melt injection within the fracture led to rapid cooling and may have promoted strength recovery and sliding arrest. Together, complete lubrication and this suction effect could influence both rupture and sliding velocities: it may favor a "pulse" rupture type (Heaton, 1990), that is, much faster and shorter sliding at a metric scale. Finally, the finding of water fossilized in a frozen mantle earthquake strongly suggests that fluid and/or hydrous minerals were present and emphasizes the need for a better understanding of their role in the mechanics of earthquakes.

Similar investigations should be directed on other outcrops within the Balmuccia peridotite, to see whether extension of this fault network can be found or not and whether the preservation state is constant along the fault or not.

Appendix A: Analytical Methods and Techniques

A1. Sample Preparation

The outcrop was sampled using a driller. The samples were cut horizontally and gradually polished to 2, 1, 0.5, and 0.1 μm. No colloidal silica was used for EBSD preparation but diluted diamond paste on soft polishing pad. For the vertical section (Figure 12), the sample was cut at 90° from the horizontal surface (Figures 4d and 4e) and endured the same preparation.

A2. Fracture Analysis

To estimate the fracture energy, we measure the cumulative length of the microfractures using scanning electron microscope imaging, as in previous studies (e.g., Griffith et al., 2010; Pittarello et al., 2012). The microfaults network is visible thanks to small offsets in crystals of the host rock, and other cracks are partly accessible thanks to amorphous filling or aligned amorphous pockets.

A3. Raman Spectrometry

The Raman spectrometer that was used in this study (Renishaw) has a wavelength of 514 nm. Amorphous pockets are basically 0.1 to 10 μm large. Only the largest ones (about 10 μm large) can be studied using the Raman beam without the signal being contaminated by the host minerals. Nevertheless, once the amorphous pockets are larger than 2 μm, the typical amorphous signal (900 to 1,100 cm^{-1}) is easily detected.

A4. Electron Backscattered Diffraction

Thanks to EBSD we evidence a clear and systematic CPO in ultramylonite-like veins, which is crucial in this study as it allows drawing the focal mechanism of the earthquake. Using EBSD, we also confirm and clarify the mineralogy down to submicrometric scale. Some amorphous pockets show devitrification when others (mostly in pyroxene grains) do not show any.

Acceleration voltage was 10 kV; beam current was 5 nA; inclination was 70°; acquisition speed was 19.21 Hz; working distance was 14 mm; step size was 0.4 μm; software used was *Aztec*; and postprocessing routine was *Channel 5*, noise reduction (every single-pixel isolated data point was removed).

Acknowledgments
We thank Damien Deldicque, Haithem Mansour, Yves Pinquier, Khaled Oubellouch, and many others for their help and support. We thank Torgeir Andersen, Giorgio Pennacchioni, and Lucas Menegon for constructive discussion that clarified our explanations. This research was funded by L'Agence Nationale de la Recherche (project "DELF" ANR12-JS06-0003 to A. S.) and the LABoratoire d'EXcellence MATISSE (UPMC—Sorbonne Universités). We thank ERC REALISM (grant 681346).

References

Aasen, H. S. (2013). Fault dynamics of pseudotachylytes in the Lindås nappe, Bergen Arcs. Unpublished Master thesis: University of Oslo, Norway. Retrieved from https://bibsys-almaprimo.hosted.exlibrisgroup.com/primo_library/libweb/action/search.do?vid=UBO

Abercrombie, R. E., & Rice, J. (2005). Can observations of earthquake scaling constrain slip weakening? *Geophysical Journal International*, *162*(2), 406–424. https://doi.org/10.1111/j.1365-246X.2005.02579.x

Andersen, T. B., & Austrheim, H. (2006). Fossil earthquakes recorded by pseudotachylytes in mantle peridotite from the Alpine subduction complex of Corsica. *Earth and Planetary Science Letters*, *242*(1-2), 58–72. https://doi.org/10.1016/j.epsl.2005.11.058

Andersen, T. B., Austrheim, H., Deseta, N., Silkoset, P., & Ashwal, L. D. (2014). Large subduction earthquakes along the fossil Moho in Alpine Corsica. *Geology*, *42*(5), 395–398. https://doi.org/10.1130/G35345.1

Andersen, T. B., Mair, K., Austrheim, H., Podladchikov, Y. Y., & Vrijmoed, J. C. (2008). Stress release in exhumed intermediate and deep earthquakes determined from ultramafic pseudotachylyte. *Geology*, *36*(12), 995–998. https://doi.org/10.1130/G25230A.1

Austrheim, H., & Andersen, T. B. (2004). Pseudotachylytes from Corsica: Fossil earthquakes from a subduction complex. *Terra Nova*, *16*(4), 193–197. https://doi.org/10.1111/j.1365-3121.2004.00551.x

Babist, J., Handy, M. R., Konrad-Schmolke, M., & Hammerschmidt, K. (2006). Precollisional, multistage exhumation of subducted continental crust. The Sesia Zone, western Alps. *Tectonics*, *25*, TC6008. https://doi.org/10.1029/2005TC001927

Beeler, N. M., Tullis, T. E., & Goldsby, D. L. (2008). Constitutive relationships and physical basis of fault strength due to flash heating. *Journal of Geophysical Research*, *113*, B01401. https://doi.org/10.1029/2007JB004988

Bestmann, M., Pennacchioni, G., Mostefaoui, S., Göken, M., & de Wall, H. (2016). Instantaneous healing of micro-fractures during coseismic slip: Evidence from microstructure and Ti in quartz geochemistry within an exhumed pseudotachylyte-bearing fault in tonalite. *Lithos*, *254*, 84–93.

Bestmann, M., Pennacchioni, G., Nielsen, S., Göken, M. & De Wall, H. (2012). Deformation and ultrafine dynamic recrystallization of quartz in pseudotachylyte-bearing brittle faults: A matter of a few seconds. *Journal of Structural Geology 38*, 21–38. https://doi.org/10.1016/j.jsg.2011.10.001

Bouchon, M., & Ihmlé, P. (1999). Stress drop and frictional heating during the 1994 deep Bolivia earthquake. *Geophysical Research Letters*, *26*, 3521–3524. https://doi.org/10.1029/1999GL005410

Boudier, F., Jackson, M., & Nicolas, A. (1984). Structural study of the Balmuccia massif (Western Alps): A transition from mantle to lower crust. *Geologie en Mijnbouw*, *63*, 179–188.

Braeck, S., & Podladchikov, Y. Y. (2007). Spontaneous thermal runaway as an ultimate failure mechanism of materials. *Physical Review Letters*, *98*(9), 095504.

Brantut, N., Han, R., Shimamoto, T., Findling, N., & Schubnel, A. (2011). Fast slip with inhibited temperature rise due to mineral dehydration: Evidence from experiments on gypsum. *Geology*, *39*(1), 59–62. https://doi.org/10.1130/G31424.1

Brantut, N., Schubnel, A., Rouzaud, J.-N., Brunet, F., & Shimamoto, T. (2008). High velocity frictional properties of a clay-bearing fault gouge and implications for earthquake mechanics. *Journal of Geophysical Research*, *113*, B10401. https://doi.org/10.1029/2007JB005551

Brantut, N., Sulem, J., & Schubnel, A. (2011). Effect of dehydration reactions on earthquake nucleation: Stable sliding, slow transients, and unstable slip. *Journal of Geophysical Research*, *116*, B05304. https://doi.org/10.1029/2010JB007876

Brodie, K. H., & Rutter, E. H. (1987). Deep crustal extensional faulting in the Ivrea Zone of Northern Italy. *Tectonophysics*, *140*(2-4), 193–212. https://doi.org/10.1016/0040-1951(87)90229-0

Chester, F. M., Chester, J. S., Kirschner, D. L., Schulz, S. E., & Evans, J. P. (2004). Structure of large-displacement, strike-slip fault zones in the brittle continental crust. *Rheology and Deformation in the Lithosphere at Continental Margins*, *1*, 223–260.

Darot, M., Guéguen, Y., Benchemam, Z., & Gaboriaud, R. (1985). Ductile-brittle transition investigated by micro-indentation: Results for quartz and olivine. *Physics of the Earth and Planetary Interiors*, *40*(3), 180–186. https://doi.org/10.1016/0031-9201(85)90128-1

Deer, W. A., Howie, R. A., & Zussman, J. (1992). *An introduction to the rock-forming minerals 696*. Hong Kong: Longman Scientific & Technical.

Del Gaudio, P., Di Toro, G., Han, R., Hirose, T., Nielsen, S., Shimamoto, T., & Cavallo, A. (2009). Frictional melting of peridotite and seismic slip. *Journal of Geophysical Research*, *114*, B06306. https://doi.org/10.1029/2008JB005990

Deseta, N., Andersen, T. B., & Ashwal, L. D. (2014). A weakening mechanism for intermediate-depth seismicity? Detailed petrographic and microtextural observations from blueschist facies pseudotachylytes, Cape Corse, Corsica. *Tectonophysics*, *610*, 138–149. https://doi.org/10.1016/j.tecto.2013.11.007

Deseta, N., Ashwal, L. D., & Andersen, T. B. (2014). Initiating intermediate-depth earthquakes: Insights from a HP–LT ophiolite from Corsica. *Lithos*, *206-207*, 127–146. https://doi.org/10.1016/j.lithos.2014.07.022

Di Toro, G., Han, R., Hirose, T., De Paola, N., Nielsen, S., Mizoguchi, K., et al. (2011). Fault lubrication during earthquakes. *Nature*, *471*(7339), 494–498. https://doi.org/10.1038/nature09838

Di Toro, G., Hirose, T., Nielsen, S., Pennacchioni, G., & Shimamoto, T. (2006). Natural and experimental evidence of melt lubrication of faults during earthquakes. *Science*, *311*(5761), 647–649. https://doi.org/10.1126/science.1121012

Di Toro, G., Nielsen, S., & Pennacchioni, G. (2005). Earthquake rupture dynamics frozen in exhumed ancient faults. *Nature*, *436*(7053), 1009–1012. https://doi.org/10.1038/nature03910

Di Toro, G., & Pennacchioni, G. (2005). Fault plane processes and mesoscopic structure of a strong-type seismogenic fault in tonalites (Adamello batholith, Southern Alps). *Tectonophysics*, *402*(1-4), 55–80. https://doi.org/10.1016/j.tecto.2004.12.036

Donaldson, C. M. (1975). Calculated diffusion coefficients and the growth rate of olivine in basaltic magmas. *Lithos*, *8*(2), 163–174. https://doi.org/10.1016/0024-4937(75)90023-7

Druiventak, A., Matysiak, A., Renner, J., & Trepmann, C. A. (2012). Kick-and-cook experiments on peridotite: Simulating coseismic deformation and post-seismic creep. *Terra Nova*, *24*(1), 62–69. https://doi.org/10.1111/j.1365-3121.2011.01038.x

Drury, M. R., Vissers, R. L. M., Van Der Wal, D., & Hoogerduijn Strating, E. H. (1991). Shear localisation in upper mantle peridotites. *Pure and Applied Geophysics*, *137*(4), 439–460. https://doi.org/10.1007/BF00879044

Ernst, W. G. (1978). Petrochemical study of lherzolitic rocks from the Western Alps. *Journal of Petrology*, *19*(3), 341–392.

Ferrand, T. P., Hilairet, N., Incel, S., Deldicque, D., Labrousse, L., Gasc, J., et al. (2017). Dehydration-driven stress transfer triggers intermediate-depth earthquakes. *Nature Communications*, *8*. https://doi.org/10.1038/ncomms15247

Freeman, J. J., Wang, A., Kuebler, K. E., Jolliff, B. L., & Haskin, L. A. (2008). Characterization of natural feldspars by Raman spectroscopy for future planetary exploration. *The Canadian Mineralogist*, *46*(6), 1477–1500. https://doi.org/10.3749/canmin.46.6.1477

Gasc, J., Hilairet, N., Yu, T., Ferrand, T. P., Schubnel, A., & Wang, Y. (2017). Faulting of natural serpentinite: Implications for intermediate-depth seismicity. *Earth and Planetary Science Letters*, *474*, 138–147. https://doi.org/10.1016/j.epsl.2017.06.016

Green, D. H., & Hibberson, W. (1970). The instability of plagioclase in peridotite at high pressure. *Lithos*, *3*(3), 209–221. https://doi.org/10.1016/0024-4937(70)90074-5

Griffith, W. A., Nielsen, S., Di Toro, G., & Smith, S. A. (2010). Rough faults, distributed weakening, and off-fault deformation. *Journal of Geophysical Research*, *115*, B08409. https://doi.org/10.1029/2009JB006925

Hacker, B., Peacock, S., Abers, G., & Holloway, S. (2003). Subduction factory 2. Are intermediate-depth earthquakes in subducting slabs linked to metamorphic dehydration reactions? *Journal of Geophysical Research*, *108*(B1), 2030. https://doi.org/10.1029/2001JB001129

Handy, M., & Zingg, A. (1991). The tectonic and rheological evolution of an attenuated cross section of the continental crust: Ivrea crustal section, southern Alps, northwestern Italy and southern Switzerland. *Geological Society of America Bulletin*, *103*(2), 236–253. https://doi.org/10.1130/0016-7606(1991)103%3C0236:TTAREO%3E2.3.CO;2

Handy, M. R., Franz, L., Heller, F., Janott, B., & Zurbriggen, R. (1999). Multistage accretion and exhumation of the continental crust (Ivrea crustal section, Italy). *Tectonics*, *18*, 1154–1177. https://doi.org/10.1029/1999TC900034

Handy, M. R., & Stünitz, H. (2002). Strain localization by fracturing and reaction weakening: A mechanism for initiating exhumation of subcontinental mantle beneath rifted margins. *Geological Society, London, Special Publications*, *200*(1), 387–407. https://doi.org/10.1144/GSL.SP.2001.200.01.22

Heaton, T. H. (1990). Evidence for and implications of self-healing pulses of slip in earthquake rupture. *Physics of the Earth and Planetary Interiors*, *64*(1), 1–20. https://doi.org/10.1016/0031-9201(90)90002-F

Hirose, T., & Shimamoto, T. (2005a). Slip-weakening distance of faults during frictional melting as inferred from experimental and natural pseudotachylytes. *Bulletin of the Seismological Society of America*, *95*(5), 1666–1673. https://doi.org/10.1785/0120040131

Hirose, T., & Shimamoto, T. (2005b). Growth of molten zone as a mechanism of slip weakening of simulated faults in gabbro during frictional melting. *Journal of Geophysical Research*, *110*, B05202. https://doi.org/10.1029/2004JB003207

Hofmann, A. W. (1980). Diffusion in natural silicate melts: A critical review. In R. B. Hargraves (Ed.), *Physics of magmatic processes* (pp. 385–417). Princeton, NJ: Princeton University Press.

Holtzman, B. K., Kohlstedt, D. L., Zimmerman, M. E., Heidelbach, F., Hiraga, T., & Hustoft, J. (2003). Melt segregation and strain partitioning: Implications for seismic anisotropy and mantle flow. *Science*, *301*(5637), 1227–1230. https://doi.org/10.1126/science.1087132

Incel, S., Hilairet, N., Schubnel, A., John, T., Ferrand, T. P., Deldicque, D., et al. (2017). Laboratory earthquakes triggered by the eclogitization of blueschist. *Earth and Planetary Science Letters*, *459*, 320–331. https://doi.org/10.1016/j.epsl.2016.11.047

John, T., Medvedev, S., Rüpke, L. H., Andersen, T. B., Podladchikov, Y. Y., & Austrheim, H. (2009). Generation of intermediate-depth earthquakes by self-localizing thermal runaway. *Nature Geoscience*, *2*, 137–140.

Kameyama, M., Yuen, D. A., & Karato, S. I. (1999). Thermal-mechanical effects of low-temperature plasticity (the Peierls mechanism) on the deformation of a viscoelastic shear zone. *Earth and Planetary Science Letters*, *168*(1-2), 159–172. https://doi.org/10.1016/S0012-821X(99)00040-0

Kanamori, H. (1977). The energy release in great earthquakes. *Journal of Geophysical Research*, *82*, 2981–2987. https://doi.org/10.1029/JB082i020p02981

Kanamori, H., Anderson, D. L., & Heaton, T. H. (1998). Frictional melting during the rupture of the 1994 Bolivian earthquake. *Science*, *279*(5352), 839–842. https://doi.org/10.1126/science.279.5352.839

Kanamori, H., & Brodsky, E. E. (2004). The physics of earthquakes. *Reports on Progress in Physics*, *67*(8), 1429–1496. https://doi.org/10.1088/0034-4885/67/8/R03

Kelemen, P. B., & Hirth, G. (2007). A periodic shear-heating mechanism for intermediate-depth earthquakes in the mantle. *Nature*, *446*(7137), 787–790. https://doi.org/10.1038/nature05717

Kirkpatrick, J. D., & Rowe, C. D. (2013). Disappearing ink: How pseudotachylytes are lost from the rock record. *Journal of Structural Geology*, *52*, 183–198. https://doi.org/10.1016/j.jsg.2013.03.003

Küster, M., & Stöckhert, B. (1999). High differential stress and sublithostatic pore fluid pressure in the ductile regime—Microstructural evidence for short-term post-seismic creep in the Sesia Zone, Western Alps. *Tectonophysics*, *303*(1-4), 263–277. https://doi.org/10.1016/S0040-1951(98)00256-X

Lahondère, D., & Guerrot, C. (1997). Datation Sm–Nd du métamorphisme éclogitique en Corse alpine: Un argument pour l'existence au Crétacé supérieur d'une zone de subduction active localisée sous le bloc corso-sarde. *Géologie de la France*, *3*, 3–11.

Le Losq, C., Neuville, D. R., Moretti, R., & Roux, J. (2012). Determination of water content in silicate glasses using Raman spectrometry: Implications for the study of explosive volcanism. *American Mineralogist*, *97*(5-6), 779–790. https://doi.org/10.2138/am.2012.3831

Lensch, G. (1971). Die Ultramafitite der Zone von Ivrea. *Annales Universitatis Saraviensis*, *9*, 5–146.

Liebske, C., Schmickler, B., Terasaki, H., Poe, B. T., Suzuki, A., Funakoshi, K.-I., et al. (2005). Viscosity of peridotite liquid up to 13 GPa: Implications for magma ocean viscosities. *Earth and Planetary Science Letters*, *240*(3-4), 589–604. https://doi.org/10.1016/j.epsl.2005.10.004

Maaløe, S. (2011). Olivine phenocryst growth in Hawaiian tholeiites: Evidence for supercooling. *Journal of Petrology*, *52*(7–8), 1579–1589. https://doi.org/10.1093/petrology/egr015

Madariaga, R. (1977). High-frequency radiation from crack (stress drop) models of earthquake faulting. *Geophysical Journal International*, *51*(3), 625–651. https://doi.org/10.1111/j.1365-246X.1977.tb04211.x

Magott, R., Fabbri, O., & Fournier, M. (2016). Subduction zone intermediate-depth seismicity: Insights from the structural analysis of Alpine high-pressure ophiolite-hosted pseudotachylyte (Corsica, France). *Journal of Structural Geology*, *87*, 95–114. https://doi.org/10.1016/j.jsg.2016.04.002

Maruyama, G., & Hiraga, T. (2017). Grain-to multiple-grain-scale deformation processes during diffusion creep of forsterite + diopside aggregate II: Grain-boundary-sliding induced grain rotation and its role in crystallographic preferred orientation in rocks. *Journal of Geophysical Research: Solid Earth*, *122*, 5916–5934. https://doi.org/10.1002/2017JB014255

Menegon, L., Pennacchioni, G., Malaspina, N., Harris, K., & Wood, E. (2017). Earthquakes as precursors of ductile shear zones in the dry and strong lower crust. *Geochemistry, Geophysics, Geosystems*, *18*, 4356–4374. https://doi.org/10.1002/2017GC007189

Mitchell, T. M., & Faulkner, D. R. (2009). The nature and origin of off-fault damage surrounding strike-slip fault zones with a wide range of displacements: A field study from the Atacama fault system, northern Chile. *Journal of Structural Geology*, *31*(8), 802–816. https://doi.org/10.1016/j.jsg.2009.05.002

Mitchell, T. M., Toy, V., Di Toro, G., Renner, J., & Sibson, R. H. (2016). Fault welding by pseudotachylyte formation. *Geology*, *44*(12), 1059–1062. https://doi.org/10.1130/G38373.1

Miyazaki, T., Sueyoshi, K., & Hiraga, T. (2013). Olivine crystals align during diffusion creep of Earth's upper mantle. *Nature*, *502*(7471), 321–326. https://doi.org/10.1038/nature12570

Mohn, G., Manatschal, G., Beltrando, M., & Haupert, I. (2014). The role of rift-inherited hyper-extension in Alpine-type orogens. *Terra Nova*, *26*(5), 347–353. https://doi.org/10.1111/ter.12104

Negrini, M., Stünitz, H., Nasipuri, P., Menegon, L., & Morales, L. F. (2014). Semi-brittle deformation and partial melting of perthitic K-feldspar: An experimental study. *Journal of Geophysical Research: Solid Earth*, *119*, 3478–3502. https://doi.org/10.1002/2013JB010573

Nielsen, S., Di Toro, G., & Griffith, W. A. (2010). Friction and roughness of a melting rock surface. *Geophysical Journal International*, *182*(1), 299–310.

Nielsen, S., Di Toro, G., Hirose, T., & Shimamoto, T. (2008). Frictional melt and seismic slip. *Journal of Geophysical Research*, *113*, B01308.

Obata, M., & Karato, S. (1995). Ultramafic pseudotachylite from the Balmuccia peridotite, Ivrea-Verbano zone, northern Italy. *Tectonophysics*, *242*(3-4), 313–328. https://doi.org/10.1016/0040-1951(94)00228-2

Ogawa, M. (1987). Shear instability in a viscoelastic material as the cause of deep focus earthquakes. *Journal of Geophysical Research*, *92*, 13,801–13,810. https://doi.org/10.1029/JB092iB13p13801

Okazaki, K., & Hirth, G. (2016). Dehydration of lawsonite could directly trigger earthquakes in subducting oceanic crust. *Nature*, *530*(7588), 81–84. https://doi.org/10.1038/nature16501

Passelègue, F., Schubnel, A., Nielsen, S., Bhat, H. S., Deldicque, D., & Madariaga, R. (2016). Dynamic rupture processes inferred from laboratory microearthquakes. *Journal of Geophysical Research: Solid Earth*, *121*, 4343–4365. https://doi.org/10.1002/2015JB012694

Peacock, S. (2001). Are the lower planes of double seismic zones caused by serpentine dehydration in subducting oceanic mantle? *Geology*, *29*(4), 299–302. https://doi.org/10.1130/0091-7613(2001)029%3C0299:ATLPOD%3E2.0.CO;2

Peč, M., Stünitz, H., Heilbronner, R., Drury, M., & de Capitani, C. (2012). Origin of pseudotachylites in slow creep experiments. *Earth and Planetary Science Letters*, *355*, 299–310.

Pennacchioni, G., & Cesare, B. (1997). Ductile-brittle transition in pre-Alpine amphibolite facies mylonites during evolution from water-present to water-deficient conditions (Mont Mary nappe, Italian Western Alps). *Journal of Metamorphic Geology*, *15*(6), 777–791. https://doi.org/10.1111/j.1525-1314.1997.00055.x

Pennacchioni, G., & Mancktelow, N. S. (2007). Nucleation and initial growth of a shear zone network within compositionally and structurally heterogeneous granitoids under amphibolite facies conditions. *Journal of Structural Geology*, *29*(11), 1757–1780. https://doi.org/10.1016/j.jsg.2007.06.002

Philpotts, A. R. (1964). Origin of pseudotachylytes. *American Journal of Science*, *262*(8), 1008–1035. https://doi.org/10.2475/ajs.262.8.1008

Philpotts, A. R. (1990). *Principles of igneous and metamorphic petrology* (p. 498). Englewood Cliffs, NJ: Prentice Hall.

Piccardo, G. B., Ranalli, G., & Guarnieri, L. (2010). Seismogenic shear zones in the lithospheric mantle: Ultramafic pseudotachylytes in the Lanzo peridotite (Western Alps, NW Italy). *Journal of Petrology*, *51*(1-2), 81–100. https://doi.org/10.1093/petrology/egp067

Pinkerton, H., & Stevenson, R. J. (1992). Methods of determining the rheological properties of magmas at sub-liquidus temperatures. *Journal of Volcanology and Geothermal Research*, *53*(1–4), 47–66. https://doi.org/10.1016/0377-0273(92)90073-M

Pittarello, L., Pennacchioni, G., & Di Toro, G. (2012). Amphibolite-facies pseudotachylytes in Premosello metagabbro and felsic mylonites (Ivrea Zone, Italy). *Tectonophysics*, *580*, 43–57. https://doi.org/10.1016/j.tecto.2012.08.001

Platt, J. D., Rudnicki, J. W., & Rice, J. R. (2014). Stability and localization of rapid shear in fluid-saturated fault gouge: 2. Localized zone width and strength evolution. *Journal of Geophysical Research: Solid Earth*, *119*, 4334–4359. https://doi.org/10.1002/2013JB010711

Prieto, G. A., Florez, M., Barrett, S. A., Beroza, G. C., Pedraza, P., Blanco, J. F., & Poveda, E. (2013). Seismic evidence for thermal runaway during intermediate-depth earthquake rupture. *Geophysical Research Letters*, *40*, 6064–6068. https://doi.org/10.1002/2013GL058109

Proctor, B., & Lockner, D. A. (2016). Pseudotachylyte increases the post-slip strength of faults. *Geology*, *44*(12), 1003–1006. https://doi.org/10.1130/G38349.1

Quick, J. E., Sinigoi, S., & Mayer, A. (1995). Emplacement of mantle peridotite in the lower continental crust, Ivrea-Verbano zone, northwest Italy. *Geology*, *23*(8), 739–742. https://doi.org/10.1130/0091-7613(1995)023%3C0739:EOMPIT%3E2.3.CO;2

Quick, J. E., Sinigoi, S., Snoke, A. W., Kalakay, T. J., Mayer, A., & Peressini, G. (2003). Geologic map of the southern Ivrea-Verbano zone, northwestern Italy. US Geological Survey.

Rempel, A. W. (2006). The effects of flash-weakening and damage on the evolution of fault strength and temperature. In R. Abercrombie, et al. (Eds.), *Radiated energy and the physics of faulting*, *Geophysical Monograph Series* (Vol. 170, pp. 263–270). Washington, DC: American Geophysical Union.

Rice, J. R. (2006). Heating and weakening of faults during earthquake slip. *Journal of Geophysical Research*, *111*, B05311. https://doi.org/10.1029/2005JB004006

Rivalenti, G., Garuti, G., & Rossi, A. (1975). The origin of the Ivrea-Verbano basic formation (western Italian Alps); whole rock geochemistry. *Società Geologica Italiana, Bollettino*, *94*, 1149–1186.

Rivalenti, G., Garuti, G., Rossi, A., Siena, F., & Sinigoi, S. (1981). Existence of different peridotite types and of a layered igneous complex in the Ivrea zone of the western Alps. *Journal of Petrology*, *22*(1), 127–153. https://doi.org/10.1093/petrology/22.1.127

Rivalenti, G., Rossi, A., Siena, F., & Sinigoi, S. (1984). The layered series of the Ivrea Verbano igneous complex, Western Alps, Italy. *Tschermaks Mineralogische Und Petrographische Mitteilungen*, *33*(2), 77–99. https://doi.org/10.1007/BF01083065

Rutter, E., Brodie, K., James, T., & Burlini, L. (2007). Large-scale folding in the upper part of the Ivrea-Verbano zone, NW Italy. *Journal of Structural Geology*, *29*(1), 1–17. https://doi.org/10.1016/j.jsg.2006.08.013

Scambelluri, M., Pennacchioni, G., Gilio, M., Bestmann, M., Plümper, O., & Nestola, F. (2017). Fossil intermediate-depth earthquakes in subducting slabs linked to differential stress release. *Nature Geoscience*, *10*(12), 960–966. https://doi.org/10.1038/s41561-017-0010-7

Schmid, S. M., Aebli, H. R., Heller, F., & Zingg, A. (1989). The role of the periadriatic line in the tectonic evolution of the Alps. In D. Dietrich & M. D. Coward (Eds.), *Alpine tectonics* (Vol. 45, pp. 153–171). London: Geological Society of London Special Publications.

Shervais, J. W. (1979). Thermal emplacement model for the Alpine Lherzolite massif at Balmuccia, Italy. *Journal of Petrology*, *20*(4), 795–820. https://doi.org/10.1093/petrology/20.4.795

Shervais, J. W., & Mukasa, S. B. (1991). The Balmuccia orogenic lherzolite massif, Italy. *Journal of Petrology*, (2), 155–174.

Sibson, R. H. (1975). Generation of pseudotachylyte by ancient seismic faulting. *Geophysical Journal of the Royal Astronomical Society*, *43*(3), 775–794. https://doi.org/10.1111/j.1365-246X.1975.tb06195.x

Silkoset, P. (2013). Microtextures of ultramafic pseudotachylyte fault veins from Corsica: an SEM-EBSD analysis. Unpublished Master thesis: University of Oslo, Norway. Retrieved from https://bibsys-almaprimo.hosted.exlibrisgroup.com/primo_library/libweb/action/search.do?vid=UBO

Sinigoi, S., Quick, J. E., Clemens-Knott, D., Mayer, A., Demarchi, G., Mazzucchelli, M., et al. (1994). Chemical evolution of a large mafic intrusion in the lower crust, Ivrea-Verbano zone, northern Italy. *Journal of Geophysical Research*, *99*, 21,575–21,590. https://doi.org/10.1029/94JB00114

Souquière, F., & Fabbri, O. (2010). Pseudotachylytes in the Balmuccia peridotite (Ivrea Zone) as markers of the exhumation of the southern Alpine continental crust. *Terra Nova*, *22*(1), 70–77. https://doi.org/10.1111/j.1365-3121.2009.00918.x

Souquière, F., Monié, P., Fabbri, O., & Chauvet, A. (2011). Polyphase seismic faulting in the Ivrea zone (Italian Alps) revealed by $^{40}Ar/^{39}Ar$ dating of pseudotachylytes. *Terra Nova*, *23*(3), 162–170. https://doi.org/10.1111/j.1365-3121.2011.00994.x

Spray, J. G. (1992). A physical basis for the frictional melting of some rock forming minerals. *Tectonophysics*, *204*(3-4), 205–221. https://doi.org/10.1016/0040-1951(92)90308-S

Spray, J. G. (1995). Pseudotachylyte controversy: Fact or friction? *Geology*, *23*(12), 1119–1122. https://doi.org/10.1130/0091-7613(1995)023%3C1119:PCFOF%3E2.3.CO;2

Sundberg, M., & Cooper, R. F. (2008). Crystallographic preferred orientation produced by diffusional creep of harzburgite: Effects of chemical interactions among phases during plastic flow. *Journal of Geophysical Research*, *113*, B12208. https://doi.org/10.1029/2008JB005618

Suzuki, A., Ohtani, E., Urakawa, S., Terasaki, H., & Kato, T. (2001). Viscosity of komatiite magma at high pressure. In *Bayerisches Forschungsinstitut für Experimentelle Geochemie und Geophysik, Universität Bayreuth Annual Report, 2001* (p. 105). Princeton University Press.

Taniguchi, H. (1992). Entropy dependence of viscosity and the glass-transition temperature of melts in the system diopside-anorthite. *Contributions to Mineralogy and Petrology*, *109*(3), 295–303. https://doi.org/10.1007/BF00283319

Trouw, R. A., Passchier, C. W., & Siersma, D. (2009). *Atlas of mylonitesand related microstructures*. Berlin: Springer Science & Business Media. https://doi.org/10.1007/978-3-642-03608-8

Ueda, T., Obata, M., Di Toro, G., Kanagawa, K., & Ozawa, K. (2008). Mantle earthquakes frozen in mylonitized ultramafic pseudotachylytes of spinel-lherzolite facies. *Geology*, *36*(8), 607–610. https://doi.org/10.1130/G24739A.1

Vetere, F., Behrens, H., Holtz, F., & Neuville, D. R. (2006). Viscosity of andesitic melts—New experimental data and a revised calculation model. *Chemical Geology*, *228*(4), 233–245. https://doi.org/10.1016/j.chemgeo.2005.10.009

Vissers, R. L. M., Platt, J. P., & van der Wal, D. (1995). Late orogenic extension of the Betic Cordillera and the Alboran domain: A lithospheric view. *Tectonics*, *14*, 786–803. https://doi.org/10.1029/95TC00086

Vitale-Brovarone, A., Beyssac, O., Malavieille, J., Molli, G., Beltrando, M., & Compagnoni, R. (2013). Stacking and metamorphism of continuous segments of subducted lithosphere in a high-pressure wedge: The example of Alpine Corsica (France). *Earth Science Reviews*, *116*, 35–56. https://doi.org/10.1016/j.earscirev.2012.10.003

White, J. C. (1996). Transient discontinuities revisited: Pseudotachylyte, plastic instability and the influence of low pore fluid pressure on deformation processes in the mid-crust. *Journal of Structural Geology*, *18*(12), 1471–1486. https://doi.org/10.1016/S0191-8141(96)00059-4

Wolff, R., Dunkl, I., Kiesselbach, G., Wemmer, K., & Siegesmund, S. (2012). Thermochronological constraints on the multiphase exhumation history of the Ivrea-Verbano zone of the Southern Alps. *Tectonophysics*, *579*, 104–117. https://doi.org/10.1016/j.tecto.2012.03.019

Xia, G. (2013). Experimental studies on dehydration embrittlement of serpentinized peridotite and effect of pressure on creep of olivine, (PhD thesis). University of California Riverside.

Yamashita, T., & Schubnel, A. (2016). Slow slip generated by dehydration reaction coupled with slip-induced dilatancy and thermal pressurization. *Journal of Seismology*, *20*(4), 1217–1234. https://doi.org/10.1007/s10950-016-9585-5

Zingg, A. (1983). The Ivrea and Strona-Ceneri Zones (Southern Alps, Ticino and N Italy); a review. *Schweizerische Mineralogische und Petrographische Mitteilungen*, *63*, 361–392.

Zingg, A., Handy, M. R., Hunziker, J. C., & Schmid, S. M. (1990). Tectonometamorphic history of the Ivrea Zone and its relation to the crustal evolution of the Southern Alps. *Tectonophysics*, *182*(1-2), 169–192. https://doi.org/10.1016/0040-1951(90)90349-D